XMM-Newton Archival Study of the ULX Population in Nearby Galaxies

Lisa M. Winter

Astronomy Department, University of Maryland, College Park, MD 20742

lwinter@astro.umd.edu

Richard Mushotzky

Goddard Space Flight Center, Greenbelt, MD 20771

richard@milkyway.gsfc.nasa.gov

Christopher S. Reynolds

Astronomy Department, University of Maryland, College Park, MD 20742

chris@astro.umd.edu

ABSTRACT

We have conducted an archival *XMM-Newton* study of the bright X-ray point sources in 32 nearby galaxies. From our list of approximately 100 point sources, we attempt to determine if there is a low-state counterpart to the Ultraluminous X-ray (ULX) population. Indeed, 16 sources in our sample match the criteria we set for a low-state ULX, namely, $L_X > 10^{38}\,\mathrm{erg\,s^{-1}}$ and a spectrum best fit with an absorbed power law. Further, we find evidence for 26 high-state ULXs which are best fit by a combined blackbody and a power law. As in Galactic black hole systems, the spectral indices, Γ, of the low-state objects, as well as the luminosities, tend to be lower than those of the high-state objects. The observed range of blackbody temperatures is 0.1-1 keV with the most luminous systems tending toward the lowest temperatures. We also find a class of object whose properties (luminosity, blackbody temperature, and power law slopes) are very similar to those of galactic stellar mass black holes. In addition, we find a subset of these objects that can be best fit by a Comptonized spectrum similar to that used for Galactic black holes in the "very high" state, when they are radiating near the Eddington limit.

Subject headings: galaxies: general — surveys — X-rays:binaries — accretion, accretion discs

1. Introduction

Through X-ray observations of nearby galaxies, a class of Ultraluminous X-ray (ULX) sources has emerged. These are pointlike, non-nuclear sources with bolometric luminosities in excess of the Eddington limit for a 20 $M_\odot$ black hole, or $L_{bol} > 2.8 \times 10^{39}$ erg s^{-1}. The true nature of these sources is unclear, and this class more likely includes several different types of objects. Though a number of these sources are located within a few parsecs of their host galaxy's dynamical center, they do not exhibit many of the characteristics of active galactic nuclei (AGN). Because the ratio of X-ray to optical flux is a factor of 10 greater than that of AGN (Anderson et al. 2003; Stocke et al. 1983), these objects are fairly easy to recognize in X-ray imaging data.

Assuming that the Eddington limit is obeyed by black hole accretion, the existence of such luminous non-AGN sources presents a puzzle. Several models have been proposed to account for the high luminosities of the ULXs. Among these are relativistic and non-relativistic beaming from stellar-mass black hole systems (Kording et al. 2002) and accretion of matter into intermediate mass black holes (IMBH). In several systems (NGC 1313 X-2, M81 X-9, etc.), detection of emission nebulae surrounding the ULX supports isotropic emission from the central source (Pakull & Mirioni 2003), which cannot be described through relativistic beaming. Further, a number of ULX (NGC1313 X-1, etc.) X-ray spectra are best fit with combined multi-component blackbody (MCD) and power law fits, similar to Galactic black holes in their high-state. Recently, Miller et al. (2003) find that many spectral fits of ULX require cool accretion disk temperatures of approximately 100 eV. The theoretical relationship between black hole mass and disk temperature (T $\propto M^{-1/4}$) has been observed to hold true for stellar mass (typically around 1 keV) and supermassive (around 10-100 eV) black holes (Makishima et al. 2000). Thus, the cool accretion disk ULXs would correspond to a population of high-state IMBHs with masses of $\approx 16 - 10^4$ $M_\odot$.

If some ULXs do indeed represent a class of high-state IMBHs, similar to the high-state stellar mass black holes in our galaxy, we might also expect to see the low-state objects from this same population. In Galactic black hole systems, the low-state is generally characterized by lower luminosity, with L< 0.1 L_{Edd} (Done & Gierlinski 2003), and a power law spectrum, typically with index $\Gamma \approx 2.0$ (McClintock & Remillard 2004). In this study we seek to find these low-state sources, classify the properties of both high-state and low-state ULXs, and examine whether these data are consistent or inconsistent with the IMBH hypothesis.

We present the results of a detailed analysis of ULXs in nearby galaxies observed with the European Space Agency's *XMM-Newton* observatory. Only *XMM-Newton* provides the count rates and bandpass necessary to distinguish different spectral models for the ULX and accurately determine both the temperature of the thermal component expected for high-state objects and whether this component is required in the spectral modeling of these objects.

In Section 2, we detail the observations examined from the *XMM-Newton* archives and explain the data analysis for the individual point sources. In Sections 3 and 4, we discuss the spectral fitting technique as well as simulations we conducted to determine their validity. We discuss the

implications of our results in Section 5.

2. Observations and Data Reduction

The data used in this investigation were drawn from the *XMM-Newton* public data archive. Assuming that low-state ULXs exist in the luminosity range of 10^{38-39} erg s^{-1}, we conducted simulations to determine the optimum criteria for observations capable of resolving point sources of this luminosity. This luminosity range was chosen on the assumption that an approximately 100 M$_\odot$ black hole would radiate at $\approx$ 5% of the L$_{Edd}$ in the low-state (Done & Gierlinski 2003). Our simulations sought to determine the number of photons required to distinguish between spectral fits using a power law model, a bremsstrahlung model, and a combined blackbody and power law model at an L$_X \sim 10^{38}$ erg s^{-1}, in addition to limiting the possibility of source confusion. We adopt these models since they qualitatively correspond to the spectra of low-state black hole X-ray binaries, neutron star X-ray binaries, and high-state black hole X-ray binaries, respectively. In order to distinguish between the different spectral fits for objects with L$_X \sim 10^{38}$ erg s^{-1}, our selection includes galaxies that were observed for at least 10 ks (with the exception of the bright ULX in NGC 5408, which had enough photons for analysis despite the low exposure time) with *XMM-Newton* and that are no more distant than 8 Mpc. This yields a minimum of 400 counts, objects with L$_X > 2 \times 10^{38}$ erg s^{-1}.

Our sample of galaxies is selective in that it represents objects of interest in the X-ray band. We include details on these host galaxies in Table 1. In most cases, the original choice to observe these galaxies (and hence their inclusion in our sample) was unlikely to be influenced by any previous knowledge of their ULX population. Hence, this sample should not be biased in terms of the ULX population. Our galaxies include only spirals and irregulars. Figure 1 displays the distribution of galaxy type.

We reduced the data using the *XMM-Newton* Science Analysis System (SAS) version 6.0.0. Since the processed pipeline products (PPS) were created with earlier versions of SAS, the observation data files (ODF) were used to produce calibrated photon event files for the EPIC-MOS and PN cameras using the commands *emchain* and *epchain*. Following this, the events tables were filtered using the standard criteria outlined in the *XMM ABC Guide*. For the MOS data (both MOS1 and MOS2 cameras), good events constitute those with a pulse height in the range of 0.2 to 12 keV and event patterns that are characterized as 0-12 (single, double, triple, and quadruple pixel events). For the PN camera, only patterns of 0-4 (single and double pixel events) are kept, with the energy range for the pulse height set between 0.2 and 15 keV. Bad pixels and events too close to the edges of the CCD chips were rejected using the stringent selection expression "FLAG == 0". Time filtering was applied as needed by editing the light curve produced in *xmmselect* for the entire observation. Flare events (distinguished by their high count rate) detected in all three cameras, were cut using the *tabgtigen* task as outlined in the *ABC Guide*. Such filtering was only done as needed.

Before extracting spectra of the brightest sources, contour maps of the X-ray observation were overlaid on Digital Sky Survey (DSS) images. This ensured that bright foreground stars and background AGN were easily distinguished, and thereby not included in the spectral fitting. Also, we checked the *XMM-Newton* positions with NED and SIMBAD to determine if they coincide with any known background galaxies or QSOs. A list of these bright fore-ground or background sources is included in Table 7.

3. Spectral Fitting

Spectra for the bright point sources were extracted using the SAS task *especget*. With this task we created spectra (for both the source and background), response matrices, and ancillary response files for all three EPIC cameras, when possible. The typical extraction radius was 20 arcseconds, but depending on both the size and proximity of a source to another source, the extraction radius ranged from 9 - 87 arcseconds. Background spectra were extracted either in an annulus centered on the source, or in a circle of appropriate size away from the source, depending on the proximity of the central source to other X-ray sources. Once the spectra were obtained, they were rebinned to require at least 20 counts per bin, using the command *grppha* in LHEASOFT. The list of sources, with position and count information, is included in Table 6.

The extracted spectra were fit with standard models in XSPEC v11.3.1. For each source, we fit the PN and MOS spectra simultaneously in the 0.3-10 keV range. We allowed a free normalization constant to account for the differences in flux calibration between the three cameras (similar to Jenkins et al. (2004)). Each source was first fit with an absorbed single component model. In all cases we used the standard absorption model *wabs*, leaving the column density as a free parameter. Results of the single-component fits are seen in Table 2. We include in this table only the best-fit parameters for those sources best described by a single-component model. The flux values quoted represent the unabsorbed flux in the PN spectra, in the 0.3-10 keV band. All errors quoted, here and subsequently, correspond to the 90% confidence level for one degree of freedom ($\Delta\chi^2 = 2.71$). The luminosities were calculated from the unabsorbed flux using the distances quoted in Table 1. Both flux and luminosity correspond to those of the best fit model (power law or bremsstrahlung). It should be noted that since our selection criteria was based on a count rate cutoff, due to the variety of spectral forms, the inferred luminosity cutoff will not be uniform.

For a number of sources, the single-component models did not adequately describe their spectra. For these sources we employed an absorbed two-component blackbody and power law model. In Table 3 we present the results of the sources best fit by this two-component fit. We include the improvement in χ^2 of the two-component fit over the simple power law. We include the power law best fits to these sources in the appendix. Table 4 includes those sources where both the single-component and two-component models were indistinguishable.

Further, for those sources we classify as ULXs (see section 5 for our criteria), we computed

bolometric luminosities. We used the exponentially cutoff power law spectrum of Magdziarz & Zdziarski (1995), model *pexrav* in *XSPEC*, with a cutoff energy of 10 keV and the reflection parameter set to zero. This model was used in place of the power law component. We computed an unabsorbed flux in the $0.1 - 100$ keV range through use of the *dummyresp* command (which extends the model beyond the observation's energy range). The luminosity was then computed using the distances listed in Table 1. We quote these values as L_{upper} in Table 5. We note that these values represent an upper limit on the bolometric luminosity for steep power law ($\Gamma > 2$) objects, since we would expect the power law component to cutoff at some low energy. However, for flat spectrum ($\Gamma < 2$) sources L_{bol} is a lower limit.

For our ULX sources modeled by a combined blackbody and exponentially cutoff power law, we estimate a more accurate L_{bol}, calculated from the flux in the range of $2 \times kT$ - 100 keV where kT is the blackbody temperature obtained from the model. In galactic X-ray binary systems, the power law component of the X-ray spectrum is believed to be from Comptonization in a corona. The photons supplying this energy originate from the blackbody continuum emanating from the accretion disk. Thus, a natural cutoff for this power law component occurs at the peak emission of the blackbody (which is approximately $3 \times kT$). These estimated blackbody values are within 95% of the full integrated blackbody flux and are therefore a good approximation to the data.

We note that our bolometric luminosities, on average, are a factor of 1.08 greater than the X-ray luminosities in the $0.3 - 10$ keV band for the objects best fit by a combined blackbody and power law. Thus, to good approximation, the X-ray luminosity is the bolometric luminosity. However, for the objects best fit by a simple power law, the average bolometric luminosity is roughly a factor of 7 greater than the X-ray luminosity in our band. This average is dominated by the steep power law objects, in particular Holmberg II XMM1 ($\Gamma = 3.09$). Excluding this object, we get an average bolometric luminosity that is 2.8 times the X-ray flux and more indicative of the general properties of these power law-fit objects.

In this large sample of point sources, we came across a number of objects whose spectra were not well fit by the standard models employed. We briefly describe these sources in the appendix.

4. Spectral Simulations

In order to determine whether the blackbody component is statistically significant for the sources fit with a two-component model, we simulated spectra of some of the brightest sources. Table 8 shows the results of these simulations. We simulated spectra using the *XSPEC* command *fakeit* for 10 bright (> 5000 counts) sources that were best fit by a combined blackbody and a power law model. The *fakeit* command uses Monte Carlo simulations in order to create a simulated spectrum from the original dataset. We simulated spectra with both 10% and 5% of the actual exposure time. These spectra were then fit with the three standard spectral fits employed in this study.

Comparing chi-square values for the simulated spectral fits, the combined blackbody and power law fit is the best fit for all simulated spectra at 10% the actual exposure time, corresponding to a source that is ten times weaker. At 5% the exposure time, 70% of the simulated spectra are well-fit by the combined model. These results suggest that indeed the blackbody component is statistically significant and distinct from a pure absorbed power law model. Thus, we are confident that the best fit for the bright combined blackbody and power law spectral fits is a valid description of the data.

5. Discussion

We have determined best-fit spectral parameters of the bright X-ray sources in 32 nearby galaxies. In choosing three "standard" models for our study, we hoped to accurately separate high and low state ULXs from other bright X-ray sources. We specifically chose to fit the data with the bremsstrahlung model in order to identify neutron star X-ray binaries within our sample.

We cross-referenced the X-ray positions of our sources with both NED and SIMBAD in order to identify known supernovae, galaxies, and stars. In addition, we examined the DSS optical images to place the position of our sources within their respective galaxies. Such analysis aimed to minimize contamination of our sample of ULXs with bright background and foreground sources.

Further, we examined *XMM-Newton's* Optical Monitor data in the visual bands (U, B, V). The PPS contain point source detection files for the OM data. We overlaid these point source detections with X-ray contour maps in order to determine the brightest possible optical count rates for the X-ray sources, which were then converted into fluxes using the OM calibration documentation. In Figure 2, we plot the distribution of the logarithm of the X-ray to optical flux for the brightest possible optical counterpart inside the *XMM-Newton* error circle. Only 13 of the 32 host galaxies had visible OM data during the observations. Of these 13 galaxies, 40 sources were in the range of the OM data and only 14 were coincident with an optical point source. Therefore, the majority of our sources have X-ray/optical flux ratios that are **larger** than those displayed. We estimate the point source detection limit of the OM U filter as approximately $1.24 \times 10^{-14} \, \mathrm{erg \, cm^{-2} \, s^{-1}}$. For an unabsorbed X-ray flux of $1.0 \times 10^{-12} \, \mathrm{erg \, cm^{-2} \, s^{-1}}$, this corresponds to $\log(f_x/f_{opt}) = 1.9$. Therefore, the average value for our sources should fall around 2 or greater. The average distribution for QSOs and AGN centers around 0 and 0.8 for BL Lacs (Anderson et al. 2003). Thus, our objects have ratios of L_x/L_{opt} atleast 10 times higher than those of AGN and 100 times greater than stars.

Recently, Gutierrez & Lopez-Corredoira (2005) identify six ULXs from the catalog of Colbert & Ptak (2002) as QSOs. They hypothesize that a large number of ULXs may in fact be quasars at higher redshift than their supposed host galaxy. However, unlike the objects studied in Gutierrez & Lopez-Corredoira (2005), our ULX sources are all spatially coincident with the optical host galaxy. In addition, a majority of our ULXs are not in the proximity of a cataloged optical point source. The X-ray/optical flux ratios of our sources are much larger, on average, than might be expected for

a QSO. It is also worth noting that while some cataloged ULXs may be QSOs, optical identifications have been made associating other ULXs with a type B supergiant companion (Kuntz et al. 2005; Liu et al. 2004).

5.1. Classification Criteria

The spectral fits indicate that we can indeed distinguish a class of low-state ULXs from the high-state objects. As a constraint on our ULX classification, we require our X-ray sources to clearly coincide with the optical extent of the host galaxy (as determined from the DSS images). Of the sources in Table 2, 16 are "low-state" objects, having unabsorbed luminosities $> 10^{38}$ erg s^{-1} and spectra that are best fit by power law models. Further, 26 sources have unabsorbed $L_X > 3 \times 10^{39}$ erg s^{-1} and spectra that are best fit by combined blackbody and power law models. These are "high-state" objects. In addition to these high and low state ULXs, we find a large number of sources best fit by a combined blackbody and power law model but below our threshold of $L_X = 3 \times 10^{39}$ erg s^{-1}. Many of these sources may be accreting stellar mass black holes. Some of these sources were found away from the optical extent of the targeted galaxy (from our analysis of the DSS images), and may represent background AGN.

5.2. Low-State ULX

For Galactic black hole X-ray binaries, spectral indices of low-state objects are typically lower than those of high-state objects (McClintock & Remillard 2004). In Figure 3, we plot the distribution of the spectral index for both high-state and low-state objects. As in the Galactic sources, it is clearly shown that the spectral indices of the high-state objects are indeed larger. Of further interest, the distribution of spectral index for low-state objects looks remarkably similar to the distribution of spectral index for moderate luminosity quasars, many of which are thought to be the analogs of low-state black holes (Porquet et al. 2004). This supports the classification of these objects as accreting black holes.

The low hard X-ray state of X-ray binaries is associated with a low accretion rate from the companion object. Therefore, on average, we expect the luminosities of the low-state objects to be lower than the high-state objects. Figure 4 displays luminosity as a function of the spectral index. On average, the highest luminosity low-state objects have luminosities lower than those of the high-state objects. We find mean values of $\Gamma = 2.46$, with a root mean square (rms) deviation of S= 0.12, and $L_X = 1.4 \times 10^{40}$ erg s^{-1}, $\log(S) = 1.6$, for the high-state objects. This calculation excludes the 3 objects with spectral indices greater than 3.5. For the low-state objects, we find mean values of $\Gamma = 2.09$, with a rms deviation of S= 0.10, and $L_X = 2.2 \times 10^{39}$ erg s^{-1}, $\log(S) = 2.1$.

The lower L_X values of the low-state objects imply that they may indeed be accreting at a lower rate than the high-state objects. This can further be seen in the bolometric luminosities

listed in Table 5. If these objects are accreting at a rate similar to galactic low-state black holes ($0.1 \times L_{Edd}$) (Done & Gierlinski 2003), we can estimate their masses as

$$\frac{M}{M_\odot} = \frac{L_{bol}}{0.1 \times L_{Edd}}$$

with L_{Edd} as the Eddington luminosity for a $1\,M_\odot$ object (1.3×10^{38} erg s^{-1}). Our mass estimations, based upon our limits to the bolometric luminosities, yield masses of $20 - 1524 M_\odot$ (see Table 5), precisely what we might expect for a population of IMBHs.

5.3. High-State ULX

If the high-state ULXs represent a class of intermediate mass black hole systems, their X-ray spectra should be best fit by a combined blackbody and power law model. Scaling for the mass of the black hole, we would expect a relationship of T $\propto$ M$^{-1/4}$ between black hole mass and blackbody temperature (Makishima et al. 2000). This would indicate a thermal component of ~ 100 eV. A few objects have been reported to display this property (Miller et al. 2003; Roberts & Warwick 2000). In Figure 5, we graph the distribution of the thermal component for our classified high-state objects.

We find that there are two peaks in the distribution among the thermal component, one at approximately 100 eV and another centered close to 1 keV. This could indicate two different classes among the high-state objects. It is possible that those objects with blackbody components near 100 eV are indeed high-state intermediate mass black holes. The second peak, centered around 1 keV, has thermal components reminiscent of the Galactic black hole systems in our own galaxy. These systems may be stellar-mass black holes accreting matter at an increased rate. If this were the case, we would expect the luminosities of the sources exhibiting a higher blackbody temperature to be lower. In the second graph of Figure 5, we plot the relationship between blackbody temperature and L$_X$ in the 0.3 - 10 keV band. Once again, two classes of ULXs are seen. The most luminous objects are those with low blackbody temperatures. On average, the less luminous sources exhibit higher blackbody temperatures.

The second, low-luminosity, class of ULX is clearly distinguishable in both plots of Figure 5. We found that, with the exceptions of NGC 253 XMM1, M81 XMM1, and NGC 5204 XMM1, the spectra of these objects could be well-described by an absorbed Comptonization (*compST*) model (Sunyaev & Titarchuk 1980) used to fit galactic black holes in the "very high" state when they are radiating at the Eddington limit. This model simulates Compton scattering of cool photons on the hot electrons of a completely ionized plasma. We present the best-fit parameters for the Comptonization model in Table 10.

This "very high" state has been observed (Miyamoto et al. 1991) in a few Galactic black holes. McClintock & Remillard (2004) use the alternative nomenclature of the steep power law state, a state which is characterized by $\Gamma > 2.4$ and a luminosity which may or may not be greater than

the luminosity in the high-state. Yet another rubric for the very high state emerged in Kubota et al. (2001) and Kubota & Makishima (2004), where they identify this as the "anomalous" state, a state whose spectrum can be well fit by an inverse Compton scattering model. Regardless of the name, our best-fit Comptonization sources likely fit into this category. The luminosities of these sources suggest that they are stellar mass black hole systems in this anomalous/very high state.

As with the low-state, we include mass estimates for our high-state objects in Table 5. We assume that the high-state objects are radiating at L_{Edd}. We find masses of $1.6 - 38\,M_\odot$ for the sources well fit by the Comptonization model. The other high-state ULXs range from $16.5 - 1354\,M_\odot$, analogous to the low-state ULX masses computed.

5.4. Temperature Gap

In addition to the existence of ULXs with low blackbody temperatures, the temperature distribution (Figure 5, left panel) displays a "gap" which is of particular interest — there is a complete absence of objects with temperatures in the range $0.26\,\mathrm{keV}$ to $0.50\,\mathrm{keV}$. It is tempting to take this as evidence for a gap in the mass distribution of these accreting black holes. Since, for a given luminosity, we expect the temperature to vary as $T \propto L^{1/4}M^{-1/2}$, this factor of two gap in the temperature distribution translates into a factor of four gap in the black hole mass distribution.

If this result is borne out by further study, it provides an important clue to the origin and evolution of intermediate mass black holes. One popular idea is that intermediate mass black holes formed from the collapse of massive Population III stars (Madau & Rees 2001). Models suggest that Pop III stars with zero age main sequence (ZAMS) masses in the range 25–$140 M_\odot$ and above $260 M_\odot$ collapse to produce black holes (Heger & Woosley 2002) whereas in the range of ZAMS masses 140–$260 M_\odot$, pair-instability supernovae lead to the complete disruption of the stars (i.e., no remnant black hole remains). Hence, this model for IMBH formation predicts a gap in the IMBH initial mass function in the range of approximately 60–$200 M_\odot$ (although this is uncertain on the low end due to the effect of the pulsational pair-instability on the pre-collapse core). One possibility is that the gap in our observed temperature distribution (and hence the inferred gap in the mass function) is due to this effect of the pair instability supernovae in Pop III stars. This would require that the current IMBH mass function is approximately the same as the initial IMBH mass function. In other words, it requires that most IMBHs (especially those just below the gap) have not grown significantly due to accretion since their formation and, hence, that the ULX phase represents a short fraction of the life-time of an IMBH ($f << t_{\mathrm{sal}}/t_{\mathrm{H}}$, where $t_{\mathrm{sal}} \approx 45\epsilon_{0.1}\,Myr$ is the e-folding timescale for Eddington limited black hole growth with radiative efficiency $\epsilon = 0.1\epsilon_{0.1}$).

An alternative interpretation of the inferred mass gap is to suppose that two fundamentally different modes of formation lead to a strong bi-modality in the final black hole mass function. Black hole masses below the gap can be readily understood through normal stellar processes. A separate and distinct population of significantly more massive black holes may result from dynamical

processes in the core of dense globular clusters (Miller & Hamilton 2002; Gültekin, Miller, & Hamilton 2004).

5.5. Galactic HMXBs

Supposing that the Galaxy's bright X-ray population is representative of low-redshift galaxies, we expected to find a number of sources similar to Galactic X-ray binaries in our sample. As previously stated, we set a luminosity cutoff of $\approx 3 \times 10^{39}$ erg s^{-1} $(0.3 - 10$ keV band) in order to distinguish between galactic HMXBs and high-state ULXs. In our sample, we find approximately 24 sources with luminosities below our high-state ULX cutoff, X-ray positions within the optical extent of their host galaxy, and no obvious optical counterpart. The unabsorbed luminosities for these sources range from $0.4 - 2.5 \times 10^{39}$ erg s^{-1} $(0.3 - 10$ keV band). Two of these sources were transients. Of the four host galaxies with multiple observations examined, two of these galaxies contained solely ULX sources in our luminosity regime (Holmberg II and NGC 5204). Each of the remaining two (NGC 253 and NGC 4258) had a transient source best fit by a combined blackbody and a power law.

This suggests an interesting diagnostic in terms of distinguishing our ULX sources from a normal HMXB population. In our own galaxy, most HMXBs vary on timescales of days or less and most of the black holes in the Milky Way are transients. The figures in a recent paper of Kalogera et al. (2004), determined through detailed mass-transfer calculations, indicate that transient behavior should not be expected from a population of IMBHs (M. Coleman Miller 2005, private communication). Thus, on average, our ULX sources should remain X-ray bright in multiple observations. Through a literature search, we found that 37/42 ULX sources are distinguishable in ROSAT observations and thus are luminous for greater than 10 years and therefore are not transients. Examination of the long term light curves show that most sources vary by less than a factor of 3 over the timescale from ROSAT to XMM.

As a possible further diagnostic, we constructed a color-color diagram for our ULX sources. We adopted the colors of Done & Gierlinski (2003) in order to compare our sample with their sample of Galactic X-ray sources. Thus, our colors were constructed from unabsorbed model fluxes in four energy bands: 3-4, 4-6.4, 6.4-9.7, and 9.7-16 keV. The *XSPEC* command *dummyresp* was used to calculate a flux based on the model for the 10-16 keV range. We plot colors for a pure unabsorbed power law (from $\Gamma = 1.5 - 3.0$) and an unabsorbed MCD model (*diskbb* in *XSPEC* with $kT_{in} = 5.0 - 0.2$ eV) for comparison. Comparing our Figure 6 with Figure 8 of Done & Gierlinski (2003), we find that our ULX sources largely lie along the same regions as their black hole sources. A few ULX sources, however, lie in the region occupied by atoll and Z-sources in the plot of Done & Gierlinski (2003). These sources were those best fit by a Comptonization model.

5.6. Galaxy Sample

It has been shown that the ULX population is proportional to the host galaxy's star formation rate (SFR) (Ranalli et al. 2002; Grimm et al. 2003). The far-infrared luminosity of a galaxy is used as an indicator of the SFR. In order to compare the ULX population of a galaxy with the SFR we followed a similar approach to Swartz et al. (2004). We calculate the FIR flux from observations taken by the *Infrared Astronomical Satellite*. As in Swartz et al. (2004), the flux between 42.4 and 122.5 μm is approximated as $1.26 \times 10^{-11}(2.58S_{60}+S_{100})$ erg cm^{-2} s^{-1}. The values of the flux at 60 μm (S_{60}) and 100 μm (S_{100}) were obtained from either Ho et al. (1997) or NED. Luminosities were calculated using the distances quoted in Table 1. We list these values in addition to the number of ULXs observed in individual galaxies in Table 11. The number of ULXs includes both the objects we classify as high and low state ULX as well as those sources resolved by Chandra.

In Figure 7, we show two plots relating the number of ULXs to L_{FIR}. It has been suggested by Grimm et al. (2003) that the luminosity function in the X-ray regime from HMXBs is related to SFR. In our first plot, we find that the galaxies with the highest L_{FIR} seem to have fewer ULXs than may be expected from the luminosity functions of Grimm et al. (2003). Thus, in a direct comparison, our results do not agree with their predictions.

The second plot displays the average number of ULXs/galaxy, binned according to luminosity. This plot is extremely similar to Fig. 15 of Swartz et al. (2004) for spiral galaxies. Thus, once again, it seems that the connection between SFR and the ULX population in spirals is supported. For irregular galaxies, however, there seems to be more of a spread in the distribution. This could be the result of poor sampling — most of the bins contain only one galaxy. Another possibility is that there is no direct correlation in irregular galaxies or that the overall star formation in these galaxies is less ordered or clumpier. If the latter is the case, the overall SFR of the galaxy is only an average over a wide range of values. We shall address this issue again in the next paper in this series (L.M. Winter et al., in preparation) where we discuss the local environment of the ULX in our sample.

In Figure 8 we plot the distribution of column densities among the ULX. We subtracted the Galactic column density towards the galaxy (obtained from the nH FTOOL and listed in Table 1) from the values obtained through spectral fits. We note that on average the ULXs have large column densities. The typical Galactic column density along a line of sight is $\approx 4 \times 10^{20}$ cm^{-2}. If the ULX is located on the opposite side of its host galaxy, we might expect maximum column densities of $\approx 1.2 \times 10^{21}$ cm^{-2}. However, most of our sources have column densities well above this value. This may imply that the local environment of the ULXs contains an extra source of absorption.

In order to better understand the relationship between SFR and the ULX population, it is necessary to extend ULX studies to other wavelengths. In particular, it becomes important to analyze UV and IR images close to the ULX.

6. Conclusion

We have found from our *XMM* survey of the ULX population in nearby galaxies that there exists a population of objects whose X-ray spectral properties closely match the low-state spectra of Galactic black holes, but whose luminosities lie in the range of $L_{bol} \approx 2 \times 10^{38} - 1 \times 10^{40}\,erg\,s^{-1}$. In the Milky Way, black holes with these spectral properties radiate at only ≈ 0.05 of the Eddington limit. If this is also true for this population, it indirectly implies that these objects have a mass greater than $\approx 30\,M_{\odot}$ ranging up to $1500\,M_{\odot}$ and thus should be IMBHs. The existence of such objects was "predicted" on the basis that the ULXs previously studied shared the X-ray spectral characteristics of high-state Galactic black holes; namely, an X-ray spectrum best fit by a combined blackbody and a power law (Miller et al. 2003), but with much higher luminosities. If these objects are high-state IMBHs, the corresponding low-state objects should also exist.

Our survey has also uncovered a large population of objects whose X-ray spectra are well modeled by the canonical description of Galactic black holes in the high-state, a black hole with a steep power law, but whose bolometric luminosities exceed $2 \times 10^{39}\,erg\,s^{-1}$, ranging up to $10^{41.5}\,erg\,s^{-1}$ and whose blackbody temperatures are less than $0.3\,keV$. If these objects are radiating at $\approx 1/2$ the Eddington limit like their Milky Way counterparts their implied masses are from $30 - 3000\,M_{\odot}$, a range very similar to that implied by the low-state objects. Using the $M^{-1/4}$ scaling of mass to temperature, the observed spectral temperatures give masses of $500 - 10^4\,M_{\odot}$ a considerably larger value. In general agreement with the expectations of the IMBH hypothesis, the objects with high-state spectra are more luminous than those with low-state spectra.

We conclude, from an X-ray spectral and luminosity point of view, that our data are consistent with many of these objects having the properties expected of an IMBH population. However, we also find two other populations of objects, those whose blackbody temperature and luminosity correspond to that of stellar mass black holes with $kT \approx 1\,keV$ and $\log L_X$ less than $2 \times 10^{39}\,erg\,s^{-1}$ and a small population of objects whose X-ray spectra and luminosities are consistent with that of stellar mass black holes in the very high state. Thus, ULX selected purely on the basis of $0.3 - 10\,keV$ X-ray luminosities are a composite class with $\approx 1/4$ being "normal" stellar mass black holes and the rest being consistent with a population of IMBHs.

The existence of a substantial population of ULXs in nearby dwarf and other low star formation rate galaxies argues that (in agreement with Ptak & Colbert (2004); Swartz et al. (2004)) there is more than one source term for the origin of ULXs, with at least some of them not being associated with recent star formation, at least statistically. We note that these results have required the high signal to noise of *XMM* in order to discern the spectrum of these objects. Many of these objects have also been observed by Chandra and their spectra have been well-fitted by simple power laws.

In a follow-up paper we will discuss the environments of these objects as revealed by *XMM* OM UV imaging and the implications this has for the origin of ULXs.

REFERENCES

Anderson, S. et al. 2003, AJ, 126, 2209

Bauer, F.E., Brandt, W.N., & Lehmer, B. 2003, AJ, 126, 2797

Brandt, W.N., Iwasawa, K., & Reynolds, C.S. 1996, MNRAS, 281, L41

Colbert, E.J.M. & Ptak, A.F. 2002, ApJS, 143, 25

Done, C. & Gierlinski, M. 2003, MNRAS, 342, 1041

Eracleous, M., Shields, J.C., Chartas, G., & Moran, E.C. 2002, ApJ, 565, 108

Freedman, W. L., et al. 1994, ApJ, 427, 628

Freeman, K. C., Karlsson, B., Lynga, G., Burrell, J. F., van Woerden, H., & Goss, W. M. 1977, A&A, 55, 445

Grimm, H.-J., Gilfanov, M., & Sunyaev, R. 2003, MNRAS, 339, 793

Guainazzi, M., et al. 2000, A&A, 356, 463

Gültekin K., Miller M.C., Hamilton D.P., 2004, ApJ, 616, 221

Gutierrez, C.M. & Lopez-Corredoira, M. 2005, preprint (astroph/0502290)

Hartwell, J., et al. 2004, MNRAS, 348, 406

Heger A., Woosley S.E., 2002, ApJ, 567, 532

Ho, L.C., Filippenko, A.V., & Sargent, W.L.W. 1997, ApJS, 112, 315

Humphrey, P.J., Fabbiano, G., Elvis, M., Church, M.J., & Balucinska-Church, M. 2003, MNRAS, 344, 134

Jenkins, L.P., Roberts, T.P., Warwick, R.S., Kilgard, R.E., & Ward, M.J. 2004, MNRAS, 349, 404

Kaaret, P., Corebel, S., Prestwich, A.H., & Zezas, A. 2003, Science, 299, 365

Kalogera, V., Henninger, M., Ivanova, N., & King, A.R. 2004, ApJ, 603, L41

Karachentsev, I.D., Sharina, M.E., Dolphin, A.E., et al. 2002, A&A, 385, 21

Kelson, D. D. 1996, ApJ, 463, 26

Kong, A.K.H. 2003, MNRAS, 346, 265

Kong, A.K.H. & Di Stefano, R. 2003, ApJ, 590, 13

Kording, E., Falcke, H., & Markoff, S. 2002, A&A, 382, L13

Kubota, A. & Makishima, K. 2004, ApJ, 601, 428

Kubota, A. et al. 2001, ApJ, 560, L147

Kuntz, K. et al. 2005, ApJ, 620, L31

Lira, P., Lawrence, A., & Johnson, R.A. 2000, MNRAS, 319, 17

Liu, J. F., Bregman, J. N., & Seitzer, P. 2004, ApJ, 602, 249

Madau P., Rees M.J., 2001, ApJ, 551, L27

Magdziarz, P. & Zdziarski, A.A. 1995, MNRAS, 273, 837

Makishima, K., et al. 2000, ApJ, 535, 632

Martin, C.L., Kobulnicky, H.A., & Heckman, T.M. 2002, ApJ, 574, 663

McClintock, J.E. & Remillard, R.A. 2004, preprint (astroph/0306213)

Miller, J. M., Fabbiano, G., Miller, M. C., & Fabian, A. C. 2003, ApJ, 585, L37

Miller M.C., Hamilton D.P., 2002, MNRAS, 330, 232

Miyamoto, S. et al. 1991, ApJ, 383, 784

Ptak, A. & Colbert, E. 2004, ApJ, 606, 291

Pakull, M.W. & Mirioni, L. 2003, RMXAA, 15, 197

Porquet, D., Reeves, J.N., O'Brien, P., & Brinkmann, W. 2004, A&A, 422, 85

Radecke, H.D. 1997, A&A, 319, 18

Roberts, T.P. & Warwick, R.S. 2000, MNRAS, 315, 98

Sakai, S., Madore, B.F., & Freedman, W.L. 1996, ApJ, 461, 713

Sakai, S. & Madore, B.F. 1999, ApJ, 526,599

Schlegel, E.M., Petre, R., Colbert, E.J.M., & Miller, S. 2000, AJ, 120, 2373

Shapley, A., Fabbiano, G., & Eskridge, P.B. 2001, ApJS, 137,139

Smith, D.A. & Wilson, A.S. 2001, ApJ, 557, 180

Stocke, J.T. et al. 1983, ApJ, 273, 458

Summers, L.K., Stevens, I.R., Strickland, D.K., & Heckman, T.M. 2003, MNRAS, 342, 690

Summers, L.K., Stevens, I.R., Strickland, D.K., & Heckman, T.M. 2004, MNRAS, 351, 1

Sunyaev, R.A. & Titarchuk, L.G. 1980, A&A, 86, 121

Swartz, D.A., Ghosh, K.K., Tennant, A.F., & Wu, K. 2004, ApJS, 154, 519

Terashima, Y. & Wilson, A.S. 2004, ApJ, 601, 735

Tolstoy, E., Saha, A., Hoessel, J.G., & McQuade, K. 1995, AJ, 110, 1640

Tosi, M., Bellazzini, M., Aloisi, A., Greggio, L., Leitherer, C., & Montegriffo, P. 2001, AJ, 122, 1271

Tully, R.B. 1988, Nearby Galaxies Catalog. Cambridge Univ. Press, Cambridge

Voges, W. et al. 1999, A&A, 349, 389

Vogler, A. & Pietsch, W. 1996, A&A, 311, 35

A.   Appendix material

The following sources were not best fit by the standard models employed in this study:

A.1.   NGC300 XMM4

This source was classified as a super-soft X-ray source by Kong & DiStefano (2003). We find that the standard single-component absorbed blackbody model is a much better model for this spectrum. In fact, the power law, bremsstrahlung, and combined models do not fit the data within the 90% confidence range. Fitting an absorbed blackbody, we find the best fit corresponds to the following parameters: $n_H = 1.38^{+0.27}_{-0.55} \times 10^{21}\,\mathrm{cm}^{-2}$, $kT = 0.059^{+0.007}_{-0.005}$, and $\chi^2/dof = 74.5/45$. This fit yields an unabsorbed flux of $3.3 \times 10^{-13}\,\mathrm{erg\,cm}^{-2}\,\mathrm{s}^{-1}$.

A.2.   NGC4631 XMM4

The spectrum of this source clearly identifies it as a super-soft X-ray source. As with NGC300 XMM4, the standard models employed in this study did not adequately match the data. The best fitting model corresponds again to an absorbed blackbody. The corresponding parameters are as follows: $n_H = 6.2^{+0.26}_{-1.5} \times 10^{21}\,\mathrm{cm}^{-2}$, $kT = 0.07^{+0.01}_{-0.01}$, and $\chi^2/dof = 142.3/74$. This fit yields an unabsorbed flux of $9.5 \times 10^{-12}\,\mathrm{erg\,cm}^{-2}\,\mathrm{s}^{-1}$. The position of this source shows it to be coincident with a globular cluster associated with that galaxy. This source was identified as a bulge X-ray source, possibly powered by accretion, in a ROSAT study of NGC4631 (Vogler & Pietsch 1996).

A.3.   NGC4631 XMM5

The spectrum of this source was best fit with an absorbed power law + an absorbed *vapec* model. This indicates the prescence of hot gas but we have no further explanation.

A.4.   NGC4945 XMM5

The spectrum of this source was not adequately fit with any of the standard models used in this investigation. The spectrum exhibits a prominent Fe K line in the PN spectrum that is well fit by a gaussian (*zgauss*) at 6.4 keV. We find that the entire spectrum is best fit with a partial covering fraction absorption model (*pcfabs*) in combination with the normal absorption, a power law, and a gaussian. The best fit parameters yield: absorption column density, $n_H = 1.79 \times 10^{21}\,\mathrm{cm}^{-2}$, partial covering absorption, $n_H = 18.4 \times 10^{21}\,\mathrm{cm}^{-2}$, partial covering fraction = 0.82, $\Gamma = 1.6$, and $\chi^2/dof = 61.8/57$. The source is clearly located within the optical galaxy, and is thus unlikely to

be a background AGN, but we have no other explanation.

A.5. M51 XMM5

The spectrum and luminosity ($L_X \approx 1.9 \times 10^{42}\,\mathrm{erg\,s^{-1}}$) of this source suggests that it is an AGN. The location of the source, from the Digital Sky Survey, places it within the dwarf companion of M51 making a value of the optical flux hard to constrain. The best fit to this source was an absorbed blackbody + power law and the spectral parameters are listed in Table 4.

A.6. M83 XMM2

Like NGC4945 XMM5, this source was best fit by a partial absorption model. However, this source showed no evidence of an Fe K line. We fit this source's spectra using a partial covering fraction absorption model in combination with the normal absorption model and a power law. The best fit parameters yield: absorption column density, $n_H = 2.1 \times 10^{21}\,\mathrm{cm^{-2}}$, partial covering absorption, $n_H = 43.5 \times 10^{21}\,\mathrm{cm^{-2}}$, partial covering fraction = 0.86, $\Gamma = 2.95$, and $\chi^2/dof = 83.5/84$. The unabsorbed flux in the range of 0.3-10 keV equals $1.37 \times 10^{-12}\,\mathrm{erg\,cm^{-2}\,s^{-1}}$.

A.7. Inverse Compton Scattering Sources

Table 7 includes the parameters for the "ULX" sources best fit by the *compST* model. A discussion of these sources and interpretation of the data is included in section 5.2.

Table 1.   *XMM-Newton* Galaxy Observations

Galaxy	Type[a]	n_H[b]	distance[c]	ref	obs id[d]	duration (s)	comments
NGC247	SAB(s)d	1.54	3.09	⋯	0110990301	14536	-
NGC253	SAB(s)c;HII	1.40	3.73	⋯	0110900101, 0152020101	30711, 110591	Starburst
NGC300	SA(s)d	3.11	2.56	⋯	0112800101	43967	-
NGC625	SB(s)m? sp; HII	2.15	2.62	⋯	0085100101	26288	-
NGC1313	SB(s)d; HII	4.0	4.17	⋯	0106860101	41310	-
IC0342	SAB(rs)cd; HII	30.3	3.9	1	0093640901	11217	-
NGC1569	IBm	21.7	1.6	1	0112290801	15582	Starburst
NGC1705	SA0- pec; HII	3.9	5.1	2	0148650101	58926	Starburst
MRK 71	BCD; HII	3.9	3.4	3	0141150201	45919	galaxy pair
NGC2403	SAB(s)cd; HII	4.15	3.56	⋯	0150651201	11415	-
Holmberg II	Im	3.42	2.70	⋯	0112520701, 0112520901	13528, 6860	-
Holmberg I	IAB(s)m	3.49	3.6	4	0026340101	26280	-
M81	SA(s)ab;LINER	4.12	3.6	4	0111800101	127913	Hol IX also in field of view
M82	I0; HII	4.14	3.9	5	0112290201	29387	Starburst
Holmberg IX	Im	4.0	3.6	4	0112521001	10350	M81 also in field of view
Sextans A	IBm	3.85	1.4	6	0026340201	21618	-
IC 2574	SAB(s)m	2.29	3.6	7	0026340301	24263	bursting star-formation
NGC 4214	IAB(s)m; HII	1.49	2.7	⋯	0035940201	14744	-
NGC 4258	SAB(s)bc;LINER	1.2	7.2	⋯	0059140901, 0110920101	16146, 21895	-
NGC4395	SA(s)m;LINER	1.33	4	⋯	0112521901	15842	-
NGC4449	IBm; HII	1.39	3.08	⋯	0112521701	15522	-
NGC4490	SB(s)d	1.78	7.8	1	0112280201	17754	interacting with NGC4485
NGC4631	SB(s)d	1.28	7.5	1	0110900201	53850	-
NGC4736	(R)SA(r)ab;LINER	1.43	4.3	1	0094360601	23461	-
NGC4945	SB(s)cd; Sy2	15.9	3.1	⋯	0112310301	23062	-
NGC 5204	SA(s)m; HII	1.42	4.8	1	0142770101, 0142770301	19205, 16387	-
M51	Sc; Sy2	1.55	7.2	1	0112840201	20924	Galaxy pair
M83	SAB(s)c;HII	3.94	6.2	⋯	0110910201	30627	Starburst
NGC5253	Im pec;HII	3.77	3.2	1	0035940301	47216	Starburst
M101	SAB(rs)cd	1.17	7.4	8	0104260101	43019	-
NGC5408	IB(s)m; HII	5.73	4.8	9	0112290601	7757	-
Circinus	SA(s)b; Sy2	57.8	4	10	0111240101	110496	-

[a]from the NASA/IPAC Extragalactic Database (NED)

[b]column density in units of $10^{20}\,cm^{-2}$, obtained from the web version of the nH FTOOL

[c]distance in Mpc (if no reference is given, obtained from the distance modulus given in LEDA)

[d]*XMM-Newton* observation ids for the data examined in this survey

References. — (1)Tully 1988; (2) Tosi et al. 2001; (3) Tolstoy et al. 1995; (4) Freedman et al. 1994; (5) Sakai & Madore 1999; (6) Sakai, Madore, & Freedman 1996; (7)Shapley, Fabbiano, & Eskridge 2001; (8) Kelson 1996; (9) Karachentsev et al. 2002; (10) Freeman et al. 1977.

Table 2. *XMM-Newton* best fit: single component spectral fits

Source	Powerlaw n_H[a]	Γ	χ^2/dof	Bremsstrahlung $\cdot n_H$[a]	kT (keV)	χ^2/dof	F_X[b]	L_X[c]
NGC247 XMM2	$1.4^{+1.8}_{-1.1}$	$2.29^{+1.02}_{-0.57}$	**47.7/54**	$0.54^{+0.11}_{-?}$g	$2.55^{+6.90}_{-1.61}$	48.8/54	0.33	0.38
NGC 253 XMM2 (obs 1)	$1.6^{+0.4}_{-0.3}$	$2.51^{+0.18}_{-0.17}$	69.1/74	$0.5^{+0.2}_{-0.3}$	$2.12^{+0.52}_{-0.37}$	74.7/74	0.52	0.87
NGC300 XMM4[d]	2.5	9.07	90.6/45	0.27	0.14	117.6/45	-	-
NGC1313 XMM4	$1.86^{+0.5}_{-0.4}$	$1.8^{+0.07}_{-0.12}$	**141.7/149**	$1.2^{+0.3}_{-0.3}$	$6.62^{+2.3}_{-1.48}$	140.1/149	0.33	0.69
IC0342 XMM1	$5.8^{+0.6}_{-0.3}$	$1.68^{+0.08}_{-0.08}$	**159.5/185**	$4.9^{+0.5}_{-0.4}$	$10.5^{+3.3}_{-1.9}$	160/185	3.5	6.37
IC0342 XMM2	$23.9^{+4.0}_{-3.6}$	$1.85^{+0.22}_{-0.20}$	**77.5/85**	$21^{+3.0}_{-2.8}$	$8.5^{+5.0}_{-2.4}$	74.9/85	4.64	8.44
IC0342 XMM4	$5.3^{+1.4}_{-1.2}$	$2.02^{+0.22}_{-0.19}$	64/58	$4.2^{+0.99}_{-0.85}$	$4.44^{+1.68}_{-0.74}$	**56.9/58**	0.69	1.26
NGC2403 XMM4	$1.7^{+0.8}_{-0.7}$	$1.89^{+0.30}_{-0.25}$	**62.3/71**	$1.1^{+0.5}_{-0.3}$	$4.59^{+4.1}_{-1.5}$	62.3/71	0.31	0.48
HolmII XMM1 (obs 2)	$1.5^{+0.2}_{-0.2}$	$3.09^{+0.15}_{-0.12}$	**266.7/252**	$0.31^{+0.12}_{-0.15}$	$1.13^{+0.11}_{-0.11}$	309.4/252	3.5	3.1
Holm I XMM2	0.35e	$2.13^{+0.16}_{-0.15}$	**39.2/45**	$?^{+?}_{-?}$	$2.5^{+0.79}_{-0.55}$	51.6/45	0.10	0.16
Holm I XMM3	0.35e	$2.05^{+0.19}_{-0.18}$	**34.4/32**	0.35e	$2.03^{+0.85}_{-0.56}$	42.1/32	0.12	0.19
IC2574 XMM1	$1.3^{+0.40}_{-0.30}$	$1.97^{+0.07}_{-0.10}$	120.9/103	$0.69^{+0.23}_{-0.25}$	$4.1^{+0.89}_{-0.67}$	**107.5/103**	0.35	0.47
IC2574 XMM2	$0.4^{+0.4}_{-0.3}$	$2.2^{+0.21}_{-0.09}$	**45.7/51**	$?^{+?}_{-?}$	$1.97^{+0.4}_{-0.3}$	57/51	0.22	0.34
NGC4214 XMM1	$1.1^{+0.52}_{-0.47}$	$1.87^{+0.26}_{-0.21}$	**41.9/38**	$0.54^{+0.41}_{-0.35}$	$4.86^{+4.52}_{-1.66}$	44.5/38	0.25	0.22
NGC4258 XMM2 (obs 2)	$6.7^{+2.6}_{-1.5}$	$2.49^{+0.44}_{-0.33}$	**83.6/57**	$4.8^{+0.9}_{-1.3}$	$2.61^{+1.22}_{-0.72}$	85.5/57	0.30	1.9
NGC4258 XMM3	$1.4^{+0.69}_{-0.64}$	$2.32^{+0.34}_{-0.24}$	**38.9/37**	$0.49^{+0.44}_{-0.38}$	$2.48^{+1.09}_{-0.74}$	41.3/37	0.20	1.2
...	3.8	1.82	**4/11**	2.7	7.14	5/11	0.077	0.48
NGC4258 XMM4	$0.68^{+0.24}_{-0.42}$	$1.97^{+0.22}_{-0.19}$	**41.1/48**	$0.06^{+0.31}_{-0.05}$	$4.07^{+1.6}_{-1.2}$	45.2/48	0.39	2.4
...	$1.9^{+0.78}_{-0.60}$	$2.24^{+0.29}_{-0.24}$	**77.03/77**	$0.9^{+0.6}_{-0.4}$	$2.82^{+1.2}_{-0.8}$	77.8/77	0.33	2.0
NGC4395 XMM2	$0.33^{+0.6}_{-0.3}$	$2.75^{+0.45}_{-0.33}$	**38.6/36**	$?^{+?}_{-?}$	$0.89^{+0.15}_{-0.14}$	50/36	0.15	0.28
NGC4395 XMM4	$0.3^{+0.6}_{-0.3}$	$2.08^{+0.39}_{-0.30}$	**16/25**	$?^{+?}_{-?}$	$2.27^{+1.16}_{-0.72}$	19.9/25	0.15	0.28
NGC4449 XMM1	$6.3^{+0.9}_{-0.7}$	$2.22^{+0.14}_{-0.12}$	**103/118**	$4.5^{+0.6}_{-0.5}$	$3.97^{+0.73}_{-0.58}$	114.3/118	1.2	1.36
NGC4449 XMM2	$1.5^{+0.3}_{-0.3}$	$2.81^{+0.16}_{-0.14}$	103.5/112	$0.25^{+0.2}_{-0.2}$	$1.65^{+0.22}_{-0.21}$	*112.1/112*	0.29	0.33
NGC4490 XMM4	$10.2^{+2.3}_{-1.8}$	$2.09^{+0.23}_{-0.19}$	*51.6/50*	$8.3^{+1.3}_{-1.5}$	$4.75^{+1.82}_{-0.90}$	50.3/50	0.84	6.1
NGC4490 XMM5	$3.9^{+0.94}_{-0.81}$	$2.31^{+0.22}_{-0.20}$	**60.1/65**	$2.5^{+0.54}_{-0.59}$	$3.08^{+0.89}_{-0.62}$	61.6/65	0.41	2.98
NGC4631 XMM4[d]	7.8	9.50	261.5/74	2.9	0.17	207.8/74	-	-
NGC4631 XMM5[f]	1.3	1.03	641.8/153	1.3	199	659/153	-	-
NGC5204 XMM2	$0.89^{+0.49}_{-0.53}$	$1.98^{+0.25}_{-0.20}$	*42.37/42*	$0.23^{+0.3}_{-0.22}$	$4.05^{+1.51}_{-0.95}$	42.2/42	0.15	0.41
...	$0.75^{+0.45}_{-0.45}$	$1.63^{+0.20}_{-0.17}$	**41.4/47**	$0.42^{+0.46}_{-0.38}$	$7.82^{+5.03}_{-2.70}$	39.4/47	0.25	0.69
M51 XMM1	$1.1^{+0.30}_{-0.27}$	$2.67^{+0.20}_{-0.16}$	**110.5/82**	$0.13^{+0.17}_{-0.13}$	$1.63^{+0.32}_{-0.25}$	140.4/82	0.34	2.8
M51 XMM3	$0.6^{+0.30}_{-0.40}$	$1.86^{+0.09}_{-0.15}$	**63.2/72**	$0.05^{+0.17}_{-0.02}$	$5.22^{+2.26}_{-1.41}$	69.2/72	0.18	1.1
M51 XMM4	$0.4^{+0.20}_{-0.30}$	$1.55^{+0.08}_{-0.13}$	**34.8/37**	$0.01^{+0.17}_{-0.13}$	$11.1^{+0.32}_{-0.25}$	34.8/37	0.16	0.99

[a] total column density in units of 10^{21} cm^{-2}

[b] unabsorbed flux in the 0.3-10 keV band in units of 10^{-12} erg cm^{-2} s^{-1}

[c] unabsorbed luminosity in the 0.3-10 keV band, using the distances quoted in Table 1, in units of 10^{39} erg s^{-1}

[d] see appendix; super-soft X-ray source best fit by single-component blackbody

[e] absorbtion column density fixed to the galactic column density found in Table 1

[f] source is best fit by a combined power law and *vapec* model; see appendix

[g] question mark denotes an error in fitting the parameter

Table 3. *XMM-Newton* best fit: two-component blackbody and power law spectral fits

Source	n_H[a]	kT (keV)	Γ	χ^2/dof	$\Delta\chi^2$[b]	F_X[c]	L_X[d]
NGC247 XMM1	$4.1^{+1.9}_{-1.5}$	$0.12^{+0.03}_{-0.02}$	$4.18^{+1.79}_{-2.52}$	86.5/93	25.7	6.2	7.1
NGC253 XMM1	$2.7^{+0.4}_{-0.4}$	$0.80^{+0.12}_{-0.09}$	$1.74^{+0.17}_{-0.14}$	225.9/230	36.7	2.7	4.5
$\cdots$	$7.3^{+1.1}_{-0.9}$	$1.14^{+0.07}_{-0.10}$	$2.54^{+0.27}_{-0.22}$	567/580	44.6	3.4	5.7
NGC253 XMM2 (obs 2)	$2.0^{+0.3}_{-0.2}$	$0.71^{+0.10}_{-0.10}$	$2.14^{+0.05}_{-0.08}$	460.3/498	47.1	1.6	2.7
NGC253 XMM3	$3.1^{+4.8}_{-0.5}$	$0.75^{+0.13}_{-0.10}$	$2.47^{+2.99}_{-0.41}$	68.5/82	23.4	0.60	1.0
$\cdots$	$3.2^{+0.7}_{-0.5}$	$0.67^{+0.13}_{-0.09}$	$2.07^{+0.14}_{-0.20}$	347.4/407	34.4	0.80	1.3
NGC253 XMM4	$20^{+10.8}_{-7.6}$	$0.11^{+0.03}_{-0.03}$	$2.51^{+0.49}_{-0.30}$	66.7/57	6.9	15	25
$\cdots$	$4.5^{+1.2}_{-1.9}$	$0.09^{+0.02}_{-0.01}$	$2.33^{+0.27}_{-0.22}$	309.3/291	12.1	1.4	2.2
NGC253 XMM5	$1.5^{+7.2}_{-1.5}$	$0.96^{+0.24}_{-0.32}$	$2.43^{+3.06}_{-1.36}$	26.5/23	5.3	0.26	0.43
$\cdots$	$4.6^{+1.1}_{-0.7}$	$0.16^{+0.02}_{-0.03}$	$1.95^{+0.14}_{-0.11}$	223.7/296	60.1	1.4	2.2
NGC253 XMM6	$6.3^{+2.1}_{-1.1}$	$0.12^{+0.02}_{-0.02}$	$2.26^{+0.18}_{-0.12}$	417.9/407	17.1	1.9	3.1
NGC253 XMM7	$6.3^{+0.9}_{-1.1}$	$0.69^{+0.11}_{-0.12}$	$2.40^{+0.41}_{-0.17}$	335.8/339	21.2	1.1	1.8
NGC300 XMM1	$1.7^{+0.20}_{-0.30}$	$0.98^{+0.14}_{-0.10}$	$3.41^{+0.06}_{-0.26}$	443.7/420	26.1	1.3	1.0
NGC300 XMM2	$3.8^{+1.7}_{-1.4}$	$0.09^{+0.01}_{-0.01}$	$2.87^{+0.34}_{-0.38}$	102.6/97	31.34	1.1	0.86
NGC300 XMM3	$4.4^{+1.0}_{-0.8}$	$0.04^{+0.25}_{-0.01}$	$1.98^{+0.1}_{-0.1}$	87.7/79	14.2	1.2	0.93
NGC300 XMM6	$2.3^{+2.6}_{-1.3}$	$0.84^{+0.25}_{-0.19}$	$4.9^{+1.97}_{-0.7}$	34.6/35	13	0.27	0.20
NGC1313 XMM1	$3.0^{+1.2}_{-0.9}$	$0.13^{+0.03}_{-0.02}$	$1.75^{+0.14}_{-0.11}$	194.1/201	35.4	0.64	1.3
NGC1313 XMM2	$3.1^{+0.4}_{-0.3}$	$0.16^{+0.04}_{-0.02}$	$2.27^{+0.10}_{-0.14}$	425.2/419	38.9	2.0	4.2
NGC1313 XMM3	$6.2^{+0.8}_{-0.6}$	$0.11^{+0.01}_{-0.01}$	$2.76^{+0.10}_{-0.11}$	441.7/424	336.6	10	22
IC0342 XMM3	$9.7^{+1.8}_{-2.1}$	$0.09^{+0.02}_{-0.01}$	$2.69^{+0.16}_{-0.23}$	129.5/107	56.3	31	56.4
NGC1705 XMM1	$0.29^{+0.39}_{-0.27}$	$1.01^{+0.41}_{-0.29}$	$2.31^{+0.89}_{-0.48}$	53/85	8.9	0.10	0.44
NGC1705 XMM2	$0.96^{+0.97}_{-0.32}$	$0.23^{+0.10}_{-0.11}$	$1.60^{+1.97}_{-0.27}$	85.5/74	6.5	0.09	0.27
NGC1705 XMM3	$0.93^{+0.51}_{-?}$e	$1.07^{+0.20}_{-0.15}$	$2.23^{+0.70}_{-0.56}$	69.8/65	11.1	0.15	0.48
MRK71 XMM1	$1.4^{+0.9}_{-0.6}$	$1.45^{+1.94}_{-0.38}$	$2.57^{+1.16}_{-0.90}$	52.6/54	4.1	0.24	0.33
NGC2403 XMM1	$2.3^{+1.2}_{-1.1}$	$0.66^{+0.16}_{-0.18}$	$2.18^{+0.41}_{-0.59}$	81.4/79	10.8	1.99	3.1
NGC2403 XMM2	$1.8^{+0.8}_{-0.6}$	$0.62^{+0.16}_{-0.11}$	$1.95^{+0.26}_{-0.42}$	163.1/151	16.4	1.0	1.6
NGC2403 XMM3	$1.7^{+1.1}_{-0.8}$	$0.74^{+0.23}_{-0.21}$	$2.15^{+0.66}_{-0.40}$	84.2/105	8.4	0.64	1.1
Holm II XMM1(obs 1)	$1.6^{+0.1}_{-0.2}$	$0.14^{+0.02}_{-0.01}$	$2.35^{+0.05}_{-0.11}$	997.5/976	136.7	12	10
Holm I XMM1	$0.4^{+0.5}_{-0.3}$	$1.97^{+0.66}_{-0.89}$	$2.46^{+0.44}_{-0.40}$	97.4/93	5.4	0.6	0.93
M81 XMM1	$3.6^{+0.07}_{-0.07}$	$0.91^{+0.02}_{-0.02}$	$2.70^{+0.04}_{-0.05}$	1316.8/1243	533.1	5.0	7.8
$\cdots$	$3.5^{+0.4}_{-0.6}$	$1.13^{+0.13}_{-0.14}$	$2.34^{+0.29}_{-0.36}$	203.5/204	21.4	4.8	7.4
M81 XMM2	$7.4^{+0.5}_{-0.7}$	$0.1^{+0.004}_{-0.004}$	$2.87^{+0.16}_{-0.17}$	833.9/616	524.3	13	22
M81 XMM3	$3.7^{+2.4}_{-2.1}$	$0.11^{+0.05}_{-0.02}$	$1.69^{+0.27}_{-0.33}$	77.1/78	4.25	0.53	0.82
M81 XMM4	$1.1^{+1.6}_{-1.0}$	$2.51^{+1.11}_{-0.73}$	$2.31^{+1.22}_{-1.05}$	48.9/50	28.2	0.43	0.70
M81 XMM5	$0.15^{+0.69}_{-0.13}$	$0.62^{+0.19}_{-0.11}$	$1.26^{+0.22}_{-0.20}$	89/80	8.5	0.38	0.59
Holm IX XMM1	$2.1^{+0.2}_{-0.2}$	$0.17^{+0.02}_{-0.02}$	$1.72^{+0.04}_{-0.03}$	866.6/878	134.3	10	16
NGC4214 XMM2	$1.8^{+1.9}_{-0.6}$	$0.81^{+0.56}_{-0.21}$	$3.95^{+1.81}_{-1.05}$	46.4/44	4.5	0.4	0.35
NGC4258 XMM1	$0.38^{+0.96}_{-0.3}$	$0.54^{+0.17}_{-0.08}$	$1.51^{+0.4}_{-0.4}$	91.1/76	10.3	0.34	2.1
NGC4258 XMM2 (obs 1)	$1.9^{+2.4}_{-0.4}$	$0.78^{+0.12}_{-0.13}$	$2.02^{+0.65}_{-1.8}$	73.4/61	24.1	0.31	1.9
NGC4395 XMM1	$2.0^{+0.08}_{-0.07}$	$0.14^{+0.02}_{-0.02}$	$3.44^{+0.54}_{-0.56}$	168.2/154	26.9	1.4	2.7
NGC4395 XMM3	$0.5^{+0.9}_{-0.3}$	$1.10^{+0.67}_{-0.18}$	$2.66^{+1.05}_{-0.77}$	52/56	3.9	0.29	0.56
NGC4449 XMM3	$3.5^{+1.3}_{-0.9}$	$0.15^{+0.03}_{-0.03}$	$2.52^{+0.36}_{-0.39}$	119.9/87	34.1	1.1	1.3
NGC4490 XMM1	$5.8^{+2.96}_{-2.96}$	$0.77^{+0.08}_{-0.095}$	$2.89^{+1.77}_{-0.61}$	66.5/63	35	0.88	6.4
NGC4490 XMM2	$4.4^{+1.9}_{-1.9}$	$0.60^{+0.20}_{-0.12}$	$2.13^{+0.50}_{-0.70}$	42.4/54	7.1	0.65	4.7
NGC4490 XMM3	$13^{+9.6}_{-2.5}$	$0.09^{+0.02}_{-0.02}$	$3.21^{+0.52}_{-0.17}$	72.1/78	4.6	12	87.4
NGC4631 XMM1	$3^{+0.9}_{-0.5}$	$0.12^{+0.03}_{-0.02}$	$2.12^{+0.03}_{-0.02}$	371.3/345	12.1	0.96	6.5

Table 3—Continued

Source	n_H[a]	kT (keV)	Γ	χ^2/dof	$\Delta\chi^2$[b]	F_X[c]	L_X[d]
NGC4631 XMM2	$2.3^{+1.4}_{-0.3}$	$0.18^{+0.05}_{-0.06}$	$1.80^{+0.12}_{-0.09}$	107.4/97	12.1	0.25	1.7
NGC4631 XMM3	$1.1^{+1.1}_{-0.8}$	$1.01^{+0.12}_{-0.1}$	$2.45^{+1}_{-0.62}$	127.1/96	18.9	0.15	1.0
NGC4945 XMM1	$3.5^{+2.1}_{-1.1}$	$0.77^{+0.27}_{-0.10}$	$1.60^{+0.40}_{-0.31}$	96.1/120	20	0.59	0.68
NGC4945 XMM2	$3.2^{+1.1}_{-0.7}$	$1.15^{+0.28}_{-0.33}$	$1.80^{+0.20}_{-0.30}$	105.8/113	8.7	0.66	0.76
NGC4945 XMM4	$4.0^{+2.0}_{-1.1}$	$0.61^{+0.10}_{-0.10}$	$2.82^{+1.06}_{-0.58}$	58.4/60	17.1	0.38	0.44
NGC5204 XMM1	$1.5^{+0.2}_{-0.2}$	$1.26^{+0.09}_{-0.09}$	$2.96^{+0.07}_{-0.08}$	551.1/559	70.3	3.0	8.3
...	$2.1^{+0.4}_{-0.2}$	$1.36^{+0.2}_{-0.17}$	$3.25^{+0.14}_{-0.12}$	566.8/496	60.1	5.3	15.0
M51 XMM2	$1.3^{+0.6}_{-0.5}$	$0.26^{+0.07}_{-0.08}$	$1.80^{+0.61}_{-0.92}$	70.7/68	4.5	0.36	3.0
M51 XMM5	$10.4^{+1.7}_{-3.7}$	$0.078^{+0.01}_{-0.01}$	$2.26^{+0.26}_{-0.25}$	59.8/70	196.2	220	1900
M51 XMM7	$2.8^{+3.4}_{-2.1}$	$0.10^{+0.03}_{-0.03}$	$1.97^{+0.43}_{-0.30}$	31.7/29	6.1	0.26	1.6
M83 XMM1	$1.4^{+0.8}_{-0.4}$	$0.50^{+0.33}_{-0.07}$	$2.22^{+0.31}_{-0.30}$	206.1/209	4.9	0.53	2.5
M83 XMM4	$0.52^{+0.16}_{-?}$	$0.56^{+0.06}_{-0.07}$	$1.52^{+0.97}_{-2.38}$	95.1/89	12.4	0.2	0.92
M101 XMM1	$0.22^{+0.12}_{-0.15}$	$0.21^{+0.03}_{-0.04}$	$1.42^{+0.14}_{-0.05}$	249.9/231	53.1	0.45	2.9
M101 XMM2	$1.6^{+0.46}_{-0.21}$	$0.76^{+0.14}_{-0.10}$	$1.88^{+0.25}_{-0.11}$	251.6/261	37.2	0.7	4.6
M101 XMM4	$1.8^{+0.17}_{-0.15}$	$0.54^{+0.11}_{-0.07}$	$2.22^{+0.12}_{-0.08}$	158.2/138	7.5	0.34	2.2
NGC5408 XMM1	$0.9^{+0.21}_{-0.16}$	$0.14^{+0.01}_{-0.01}$	$2.71^{+0.16}_{-0.20}$	316.4/337	80.4	3.97	10.9
CIRCINUS XMM1	$10.1^{+1.2}_{-1.2}$	$0.10^{+0.01}_{-0.01}$	$2.30^{+0.08}_{-0.08}$	749.4/861	13.5	12	23
CIRCINUS XMM2	$11.2^{+2.4}_{-1.7}$	$0.53^{+0.03}_{-0.03}$	$4.71^{+0.94}_{-0.49}$	438.5/430	79.4	5.6	10.7
CIRCINUS XMM3	$13.5^{+5.5}_{-5.6}$	$0.67^{+0.10}_{-0.08}$	$5.77^{+2.24}_{-2.3}$	269.3/260	15.9	7.6	14.5

[a]total column density in units of 10^{21} cm^{-2}

[b]improvement in χ^2 over the single-component power law model

[c]unabsorbed flux in the 0.3-10 keV band in units of 10^{-12} erg cm^{-2} s^{-1}

[d]unabsorbed luminosity in the 0.3-10 keV band, using the distances quoted in Table 1, in units of 10^{39} erg s^{-1}

[e]question mark denotes an error in fitting the parameter

Table 4. *XMM-Newton* best fit single/two-component spectral fits

Source	power law			blackbody and power law					
	n_H[a]	Γ	χ^2/dof	n_H[a]	kT (keV)	Γ	χ^2/dof	F_X[c]	L_X[d]
NGC300 XMM5	$?^{+?}_{-?}$e	$2.1^{+0.15}_{-0.11}$	49.3/55	$0.41^{+0.60}_{-0.30}$	$1.06^{+0.37}_{-0.20}$	$2.78^{+0.61}_{-0.65}$	47.3/53	0.17	0.13
Sextans A XMM1	$0.18^{+0.23}_{-0.16}$	$2.25^{+0.12}_{-0.07}$	271.4/275	$0.4^{+0.7}_{-0.1}$	$1.05^{+2.3}_{-0.07}$	$2.6^{+0.8}_{-0.2}$	269.1/271	0.60	0.14
IC2574 XMM3	$0.15^{+0.35}_{-0.14}$	$2.43^{+0.27}_{-0.18}$	40.3/49	$1.1^{+0.6}_{-0.8}$	$0.87^{+1.59}_{-0.21}$	$3.56^{+0.99}_{-0.90}$	38.4/47	0.36	0.56
NGC4736 XMM1	$0.95^{+0.6}_{-0.5}$	$2.02^{+0.26}_{-0.25}$	62.8/53	$6.3^{+3.0}_{-3.7}$	$0.08^{+0.03}_{-0.02}$	$2.41^{+0.34}_{-0.27}$	54.9/51	8.1	17.9
NGC4945 XMM3	$3.3^{+1.3}_{-0.9}$	$1.82^{+0.12}_{-0.20}$	30.8/30	$6.8^{+4.3}_{-4.5}$	$0.11^{+0.09}_{-0.05}$	$2.03^{+0.22}_{-0.69}$	29.7/28	0.95	1.09
M51 XMM6	$2.0^{+0.83}_{-0.72}$	$2.50^{+0.33}_{-0.25}$	40.97/43	$8.2^{+3.5}_{-5.6}$	$0.08^{+0.05}_{-0.02}$	$3.0^{+0.37}_{-0.43}$	36.9/41	5.6	35
M101 XMM3	$1.5^{+0.4}_{-0.3}$	$2.70^{+0.21}_{-0.17}$	130.3/133	$1.6^{+0.3}_{-0.1}$	$0.64^{+0.14}_{-0.12}$	$2.93^{+0.3}_{-0.8}$	129.9/131	0.56	3.7
M101 XMM5	$1.3^{+0.2}_{-0.3}$	$2.28^{+0.12}_{-0.11}$	47.9/46	$1.3^{+1.2}_{-0.2}$	$0.18^{+0.05}_{-0.06}$	$1.95^{+0.3}_{-0.22}$	45.1/44	0.13	0.85

[a]total column density in units of 10^{21} cm^{-2}

[b]improvement in χ^2 over the single-component power law model

[c]unabsorbed flux in the 0.3-10 keV band in units of 10^{-12} erg cm^{-2} s^{-1} for combined fit

[d]unabsorbed luminosity in the 0.3-10 keV band, using the distances quoted in Table 1, in units of 10^{39} erg s^{-1}

[g]question mark denotes an error in fitting the parameter

Table 5.   Bolometric Luminosities of ULX sources

Source	L_{upper}[a]	L_{bol}[b]	M_{Edd}[c]
NGC247 XMM1	13.4258	7.07734	54.4411
NGC253 XMM1	9.31469	2.44574	18.8134
NGC253 XMM2	4.3701	2.15292	16.561
NGC253 XMM6	5.05828	3.92514	30.1934
NGC1313 XMM3	37.0364	27.9692	215.148
NGC1313 XMM4	1.50345	$\cdots$	115.65
IC0342 XMM1	14.1215	$\cdots$	1086.27
IC0342 XMM2	19.8129	$\cdots$	1524.07
IC0342 XMM3	114.015	95.4068	733.899
NGC2403 XMM1	4.1497	2.14873	16.528
NGC2403 XMM4	0.57068	$\cdots$	43.898
Holmberg II XMM1	0.88906	$\cdots$	68.3893
$\cdots$	16.8335	11.4543	88.1103
Holmberg I XMM2	10.5158	$\cdots$	808.908
M81 XMM1	15.7004	3.17932	24.4563
Holmberg IX XMM1	31.0582	28.1445	216.496
NGC4214 XMM1	0.26699	$\cdots$	20.5379
NGC4258 XMM3	0.46503	$\cdots$	35.7715
NGC4395 XMM1	9.04609	2.94683	22.6679
NGC4449 XMM1	2.11312	$\cdots$	162.547
NGC4449 XMM2	2.48586	$\cdots$	191.22
NGC4490 XMM1	16.8513	3.21972	24.7671
NGC4490 XMM2	7.36612	4.51554	34.7349
NGC4490 XMM3	240.653	176.04	1354.15
NGC4490 XMM4	1.66829	$\cdots$	128.33
NGC4490 XMM5	12.7136	$\cdots$	977.971
NGC4631 XMM1	10.6527	8.59661	66.1278
NGC4736 XMM1	31.6561	27.3664	210.511
NGC5204 XMM1	22.4756	2.20492	16.9609
NGC5204 XMM2	5.57769	$\cdots$	429.053
M51 XMM1	4.76208	$\cdots$	366.314
M51 XMM2	4.25898	3.57502	27.5001
M51 XMM3	2.10133	$\cdots$	161.641
M51 XMM4	2.56064	$\cdots$	196.972
M51 XMM6	46.7642	39.5189	303.991
M101 XMM1	8.04916	7.68224	59.0942
M101 XMM2	7.54268	4.96709	38.2084
M101 XMM3	10.9792	1.03659	7.97381
NGC5408 XMM1	20.9211	11.5369	88.7455
Circinus XMM1	70.3579	56.1033	431.564
Circinus XMM2	208.746	0.69929	5.37916
Circinus XMM3	771.157	0.212957	1.63813

[a]upper limit on the bolometric luminosity, determined with an exponential cut-off in the power law at high energy (see text)

[b]bolometric luminosity estimate for high-state ULXs where the power law is cut at twice kT_{in} (see text); units

for both luminosity measurements in 10^{39} erg s^{-1}

[c]mass computed for objects radiating at $0.1 \times L_{Edd}$ (low-state objects) or L_{Edd} (high-state objects; using L_{bol}), in units of $M_{\odot}$

Table 6. Bright Point Sources examined

Source[1]	RA (h m s)	Dec (° ′ ″)	Total Counts	Count Rate[2]	ID	Location in galaxy[3]
NGC247 XMM1	00 47 03.8	-20 47 46.2	3458, 1389, 1379	20.33, 5.8, 6.4	1RXS J004704.8-204743	sa
NGC247 XMM2	00 47 03.1	-20 37 02.5	-, 597, 600	-, 1.9, 1.4	-	sa
NGC253 XMM1	00 47 32.8	-25 17 52.6	-, 3156, 2985	-, 11.38, 9.9	NGC253 PSX-2[4]	near center
...	...	...	-, 12654, 12812	-, 8.7, 9.1	-	-
NGC253 XMM2	00 47 22.4	-25 20 55.2	-, 825, 942	-, 2.8, 2.97	NGC253 PSX-5	sa
...	...	...	-, 10347, 10304	-, 8.2, 8.5	...	-
NGC253 XMM3	00 47 35.2	-25 15 13.8	-, 870, 1065	-, 3, 3.41	NGC253 PSX-7	sa
...	...	...	-, 5988, 6131	-, 4.2, 4.6	-	-
NGC253 XMM4	00 47 23.3	-25 19 06.5	-, 649, 703	-, 1.4, 1.3	-	sa
...	...	...	-, 3823,3738	-, 1.7, 1.95	-	-
NGC253 XMM5	00 47 17.6	-25 18 12.1	-, 295, 313	-, 1.08, 1.04	NGC253 PSX-4	sa
...	...	...	-, 4199, 4303	-, 3.6, 3.8	...	-
NGC253 XMM6	00 47 42.8	-25 15 05.5	-, 6081, 6407	-, 3.8, 4.4	NGC 0253 [VP99] X40	sa
NGC253 XMM7[5]	00 47 09.2	-25 21 21.7	-, 4300, 4454	-, 2.6, 3.0	-	sa
NGC300 XMM1	00 55 09.9	-37 42 13.9	6778, 2248, 2453	18.6, 4.9, 5.4	-	edge sa?
NGC300 XMM2	00 55 10.6	-37 48 36.7	1364, 456, 463	3.1, 0.9, 0.9	-	sa[6]
NGC300 XMM3	00 54 49.7	-37 38 53.8	915, 442, 435	2.2, 0.9, 0.9	-	sa
NGC300 XMM4	00 55 10.9	-37 38 53.8	745, 224, 233	1.9, 0.3, 0.4	XMMU J005511 -3749; SSS[7]	out
NGC300 XMM5	00 55 21.1	-37 29 19.5	750, 247, 250	1.7, 0.4, 0.5	-	out
NGC300 XMM6	00 54 44.2	-37 51 04.5	517, 187, 165	1.1, 0.3, 0.3	-	sa
NGC625 XMM1[8]	01 35 06.8	-41 26 17.1	5832, 577, 2119	3, 0.6, 1.4	-	sa
NGC1313 XMM1	03 18 19.9	-66 29 10.7	2876, 900, 810	8.6, 3.2, 2.8	NGC1313 [CPS95] X-1	edge sa
NGC1313 XMM2	03 17 38.8	-66 33 05.3	7568, 2357, 2108	25.4, 8.8, 7.8	NGC1313 [CPS95] X-3; SN 1978 K	edge sa?
NGC1313 XMM3	03 18 22.5	-66 36 06.2	6960, 2179, 1793	23.3, 8.1, 6.6	NGC1313 [CPS95] X-2	near center
NGC1313 XMM4	03 18 18.5	-66 30 05	2075, 659, 567	5.1, 1.8, 1.5	NGC1313 [SPC2000] X-8	sa
IC0342 XMM1	03 45 55.8	+68 04 54.5	1802, 1216, 1105	33.6, 12.4, 11.1	IC0342 [RW2000] X-1	sa
IC0342 XMM2	03 46 15.0	+68 11 11.2	1147, 541, 184	21.1, 5.5, 1.7	IC0342 [RW2000] X-3	near center
IC0342 XMM3	03 46 48.6	+68 05 43.2	1186, 670, 606	21.7, 6.8, 6.0	IC0342 [LLJ2000] X-2	near center
IC0342 XMM4	03 46 57.2	+68 06 20.2	551, 338, 377	9.5, 3.9, 3.6	IC0342 [RW2000] X-6	...
NGC1569[9]	...	...			...	out?
NGC1705 XMM1	04 54 57.6	-53 24 23.5	1174, 400, 371	2.4, 0.6, 0.6	RX J0454.9-5324	out?
NGC1705 XMM2	04 54 19.6	-53 20 41.9	933, 375, 397	1.9, 0.6, 0.6	...	out?
NGC1705 XMM3	04 54 38.1	-53 18 16.2	698, 372, 418	1.4, 0.6, 0.6	WGA J0454.7-5318	out
MRK71 XMM1	07 28 51.8	+69 07 27	832, 225, 207	3.9, 0.97, 0.9	-	edge sa
NGC2403 XMM1	07 36 25.6	+65 35 40	-, 1199, 672	-, 1.0, 0.60	NGC2403 [RW2000] X-1	

Table 6—Continued

Source[1]	RA (h m s)	Dec (o ′ ″)	Total Counts	Count Rate[2]	ID	Location in galaxy[3]
NGC2403 XMM2	07 36 50.2	+65 36 02.1	1964, 729, 672	1.99, 0.63, 0.60	-	near center
NGC2403 XMM3	07 36 55.4	+65 35 40.3	1497, 489, 378	1.4, 0.40, 0.33	-	near center
NGC2403 XMM4	07 37 02.5	+65 39 35.2	1004, 274, 288	0.52, 0.15, 0.21	NGC2403 [RW2000] X-4	edge sa?
Hol II XMM1	08 19 28.8	+70 42 20.3	31052, 1257, 10807	272.2, 75.5, 72.7	Holm II X-1; IXO 31[10]	near center?
...	...	...	3853, 1361, 1452	78.3, 18.9, 20.5	...	
Hol I XMM1	09 41 30	+71 12 34	687, 768, 754	2.9, 2.7, 2.6		out?
Hol I XMM2	09 39 59.7	+71 06 40.2	575, 203, 224	2.5, 0.7, 0.7	1WGA J0940.0+7106	out?
Hol I XMM3	09 42 06.7	+71 04 45.3	452, 141, 141	1.7, 0.4, 0.4	-	out?
M81 XMM1	09 55 32.9	+69 00 34.8	50788, -, 18988	51.1, -, 21.7	M81 [F88] X-6; NGC3031 [RW2000] X-11	sa
...	...	...	-, 1227, -[11]	-, 12, 13.1	...	
M81 XMM2	09 55 24.8	+69 01 11.7	17871, -, 4121	13.2, -, 4.4	SN 1993J	sa
M81 XMM3	09 55 10.6	+69 05 02.2	-, -, 1970	-, -, 1.5	-	sa
M81 XMM4	09 55 24.3	+69 10 00.2	-, -, 1197	-, -, 1.0		edge sa
M81 XMM5	09 55 49.2	+69 05 30.5	-, -, 2077	-, -, 2.3		sa
M82[12]			...	...	...	...
Hol IX XMM1	09 57 53.3	+69 03 48.7	14976, 6546, 6586	207.3, 64.3, 65	Hol IX X-1; IXO 34	?
Sextans A XMM1	10 11 24.6	-04 42 17.2	3963, 1323, 1242	17.2, 5, 4.5	-	out
IC2574 XMM1	10 28 42.4	+68 28 17.8	1047, 673, 623	8.3, 2.6, 2.5		sa
IC2574 XMM2	10 26 33.5	+68 29 32.1	533, 335, 300	4.3, 1.3, 1.2		out
IC2574 XMM3	10 27 22.2	+68 18 47.6	538, 293, 301	4.2, 1.1, 1.2		out
NGC4214 XMM1	12 15 37.0	+36 19 29.4	434, 230, 225	2.9, 1.6, 1.5	NGC4214 [HSS2004] 11	sa
NGC4214 XMM2	12 15 58.2	+36 22 38.5	626, 160, 285	3.4, 0.6, 1.5	-	out
NGC4258 XMM1[5]	12 18 47.8	+47 20 51.7	828, 470, 444	7.0, 2.8, 2.8	-	sa
...	...	...	...	...	...	
NGC4258 XMM2	12 18 57.8	+47 16 06.8	732, 337, 337	5.8, 2, 2.1	NGC4258 [RW2000] X-7	sa
...	...	...	716, 268, 290	1.8, 1, 1.0	...	
NGC4258 XMM3	12 18 56.5	+47 21 24.3	489, 182, 184	3.8, 0.9, 1.1	NGC4258 [RW2000] X-5	sa
...	...	...	-, 160, 142	-, 0.3, 0.3	...	
NGC4258 XMM4	12 19 23.2	+47 09 37.2	644, 277, 224	4.9, 1.3, 1.3	HELLAS 288	edge sa?
...	...	...	964, 410, 382	0.3, 0.2, 0.1	...	
NGC4395 XMM1	12 26 01.5	+33 31 29	2162, 862, 921	15.5, 5.1, 5.6	NGC4395 [RW2000] X-1; IXO 53	sa
NGC4395 XMM2	12 25 25.3	+33 36 46.4	392, 252, 208	2.6, 1.5, 1.2	-	sa?
NGC4395 XMM3	12 25 32.6	+33 25 27.9	763, 277, 278	5.2, 1.5, 1.6	-	out?
NGC4395 XMM4	12 25 42.7	+33 40 00.1	516, 60, 40	3.1, 0.3, 0.2		out
NGC4449 XMM1	12 28 18	+44 06 30.9	1409, 608, 593	10.6, 3.6, 3.5	XRB?; NGC4449 [RW2000] X-7; Source 27[13]	sa

Table 6—Continued

Source[1]	RA (h m s)	Dec (o ′ ″)	Total Counts	Count Rate[2]	ID	Location in galaxy[3]
NGC4449 XMM2	12 28 09.3	+44 05 03.9	1503, 527, 586	11.3, 3.1, 3.5	SNR?; NGC4449 [RW2000] X-1; Source 10	sa
NGC4449 XMM3	12 28 11.1	+44 06 43.9	1094, 549, 404	8.3, 3.2, 2.3	SNR; Source 15	sa
NGC4490 XMM1	12 30 32.4	+41 39 14.6	746, 323, 393	6.0, 1.9, 2.2	NGC4490 [RW2000] X-1	near center
NGC4490 XMM2	12 30 36.5	+41 38 33.3	656, 299, 310	5.3, 1.7, 1.7	NGC4490 [RW2000] X-2	sa
NGC4490 XMM3	12 30 43.3	+41 38 11.5	832, 501, 461	5.8, 2.6, 2.2	NGC4490 [RW2000] X-4	sa
NGC4490 XMM4	12 30 31.1	+41 39 08.1	546, 291, 286	4.4, 1.7, 1.6	CXOU J123030.8 +413911	sa
NGC4490 XMM5	12 30 30.3	+41 41 40.3	413, 587, 482	2.7, 3.1, 2.3	NGC4485 [RW2000] X-1	sa
NGC4631 XMM1	12 41 55.8	+32 32 14	5093, 1969, 1762	13, 4.2, 3.8	NGC4631 [RW2000] X-1; IXO 68	sa
NGC4631 XMM2	12 41 57.5	+32 32 01	1273, 531, 400	3.3, 1.2, 0.9	NGC4631 [RW2000] X-2	out
NGC4631 XMM3	12 41 58.2	+32 28 49.6	1271, 443, 457	2.8, 0.9, 0.9	CXOUSEXSI J124158.0+322851	sa
NGC4631 XMM4	12 42 16.1	+32 32 48.8	957, 400, 429	2.3, 0.8, 0.8	[VP96] H13	sa
NGC4631 XMM5	12 42 11.2	+32 32 33.6	1626, 894, 866	3.9, 1.9, 1.8	[VP96] H12; [HFE2003] PSX-01	near center
NGC4736 XMM1	12 50 50.2	+41 07 12	713, 273, 227	6.7, 2.1, 1.7	NGC4736 X-4[14]	sa
NGC4945 XMM1	13 05 33.3	−49 27 36.3	1456, 646, 595	7.9, 2.9, 2.6	NGC4945 [GMB2000] X-2	sa
NGC4945 XMM2	13 05 38.4	−49 25 45.3	1393, 600, 523	7.6, 2.7, 2.3	NGC4945 [R97] X-3	sa
NGC4945 XMM3	13 05 18.8	−49 28 24	-, 357, 362	-, 1.6, 1.6	...	sa
NGC4945 XMM4	13 05 22.2	−49 28 26.3	731, 331, 332	4.0, 1.5, 1.5	NGC4945 [BIR96] X-1?	sa
NGC4945 XMM5	13 05 25.7	−49 28 30.7	772, 267, 301	4.2, 1.2, 1.32	...	sa
NGC5204 XMM1	13 29 38.5	+58 25 03.6	9981, 3352, 3384	62.8, 17.7, 17.9	NGC5204 [RW2000] X-1; IXO 77	-
⋮			9231, 2284, 2349	85.5, 24.7, 25.8		edge sa
NGC5204 XMM2	13 29 27.4	+58 25 31.8	573, 170, 231	3.4, 0.8, 1.2		-
⋮			772, 161, 121	5.0, 1.7, 1.1		
M51 XMM1	13 29 40	+47 12 36.2	1102, 367, 409	6.2, 1.8, 2	NGC5194 [RW2000] X-1	sa
M51 XMM2	13 30 07.7	+47 11 04.8	514, 540, 549	2.6, 2.2, 2.2	IXO 81	sa
M51 XMM3	13 30 01.1	+47 13 41.4	1004, 315, 311	4.1, 1.1, 1.1	CXOU J133001.0 +471344; IXO 80	sa
M51 XMM4	13 30 06	+47 15 38.9	518, 183, 166	2.8, 0.9, 0.8	NGC 5195 [RW2000] X-1	near center
M51 XMM5	13 29 59.6	+47 15 54	1079, 359, 257	5, 1.5, 1	CXOU J132959.5 +471559	sa
M51 XMM6	13 29 57.5	+47 10 45.3	536, 206, 247	1.9, 0.6, 0.8	CXOU J132957.6 +471048	edge sa
M51 XMM7	13 29 53.6	+47 14 31.5	452, 141, 143	2.4, 0.6, 0.7	CXOU J132953.7 +471436	sa
M83 XMM1	13 37 19.8	−29 53 49.8	3074, 927, 987	12, 3.3, 2.5	RX J133719 -2953.6; IXO 82	sa
M83 XMM2	13 36 59.4	−29 49 57.2	1133, 371, 397	4, 1.3, 1	CXOU J133659.4 -294959	sa
M83 XMM3[15]	13 37 04.4	−29 51 24	1724, 576, 459	7.2, 2.3, 1.2	CXOU J133704.3 -295121	sa
M83 XMM4	13 37 01.5	−29 53 26	1289, 345, 401	4.9, 1.3, 1.0	CXOU J133701.4 -295326	sa
NGC5253[16]	...	...	...	...	...	...
M101 XMM1	14 03 14.7	+54 18 05	2690, 1449, 1417	10.3, 3.3, 3.3	CXOU J140313.9 +541811; XMM-2[17]	sa

Table 6—Continued

Source[1]	RA (h m s)	Dec (o ' '')	Total Counts	Count Rate[2]	ID	Location in galaxy[3]
M101 XMM2	14 03 03.8	+54 27 37	2825, 1623, 1551	10.3, 3.6, 3.3	XMM-1	edge sa?
M101 XMM3	14 04 14.6	+54 26 04.4	1460, 822, 717	5, 1.6, 1.3	CXOU J140414.3 +542604; XMM-3	edge sa?
M101 XMM4	14 02 28.5	+54 16 26.7	1505, 877, 757	5.1, 1.7, 1.5	CXOU J140228.3 +541626	sa
M101 XMM5	14 02 22.5	+54 17 58	516, 245, 289	1.8, 0.4, 0.6	CXOU J140222.2 +541756; XMM-6	sa
NGC5408 XMM1	14 03 19.8	-41 22 59.3	5932, 2036, 2077	12.8, 3.2, 3.3	NGC5408 [KCP2003] X-1	sa
CIRCINUS XMM1[18]	14 12 54.2	-65 22 55.3	16220, 11452, -	14.5, 11.3, -	-	edge sa?
CIRCINUS XMM2	14 12 39.2	-65 23 34.3	8741, 2386, -	5.7, 1.9, -	-	edge sa?
CIRCINUS XMM3	14 13 28.3	-65 18 08.3	4873, 1031, -	1.8, 0.7, -	-	edge sa?

[1] Sources labeled XMM-n in order of apparent brightness from the first observation studied

[2] count rate units of $\times 10^{-2}$ cts s^{-1} for the PN, MOS1, and MOS2 spectra

[3] ocation specified as: inside the optical extent of the galaxy or in spiral arms (sa), near the center of the galaxy, at the edge of a spiral arm/ optical extent of galaxy, or outside the optical extent of the galaxy. Location based on DSS images.

[4] identification for NGC0253 following Humphrey et al. (2003)

[5] Transient.

[6] Appears as an extended source in HST image.

[7] Kong & DiStefano 2003

[8] Spectra too scattered to model.

[9] bright sources coincide with nucleus (unresolvable star cluster and X-ray binaries), fore-ground star, and background AGN (Martin, Kobulnicky, Heckman (2002)

[10] IXO designation from Colbert & Ptak (2002)

[11] Spectrum from Hol IX observation.

[12] bright source is too close to other sources

[13] Chandra observations of point sources in NGC4449 published in Summers et al. (2003); Source 27 varied from ROSAT observations

[14] three other sources near the nucleus are unresolveable in the XMM obs., but seen by Chandra (Eracleous et al. 2002)

[15] Unable to model sprectrum due to an error in χ^2-space

[16] bright sources are too close, but resolvable by Chandra (Summers et al. 2004)

[17] alternate ID from Jenkins et al. (2004)

[18]bright sources near the nucleus are unresolvable, but seen by Chandra (Smith & Wilson 2001)

Table 7. Bright, Identifiable Background and Foreground Sources

Galaxy	RA (h m s)	Dec (o ′ ″)	Identification
NGC 247	0 46 51.7	-20 43 30	QSO B044-2059
NGC 300	0 55 26.7	-37 31 25.6	HD 5403 (Star)
NGC 625	01 34 42.4	-41 36 15.2	QSO B0132-4151
NGC 1569[a]	04 31 16.9	+64 49 50	CXOU J043116.8+644950 (Star)
NGC 1569	04 31 14.2	+64 51 07.9	CXOU 043114.0+645107 (Star)
NGC 1569	04 31 25.4	+64 51 53.8	CXOU 043125.1+645154 (AGN)
NGC 1705	04 54 01.2	-53 21 12.3	WGA J0454.0-5320 (M star or elliptical galaxy)
NGC 2403	07 35 09	+65 40 27.5	HD 59581 (Star)
NGC 4258	12 18 08.9	+47 16 08.3	QSO J1218+472
M83	13 36 45.6	-29 59 13.9	2MASX J13364579-2959122 (Galaxy)
M83	13 36 13.9	-29 56 13	RX J133615-2957.8 (Galaxy)
NGC 5253	13 39 50.6	-31 34 11.1	CD-30 10790 (Star)
M101	14 02 30	+54 21 18.2	[WIP99] H13 (Star)[b]
NGC 5408	14 03 27.5	-41 25 18.5	(Star)

[a]identification for objects in NGC 1569 from Martin, Kobulnicky, & Heckman (2002)

[b]confirmed by K. Kuntz using HST ACS

Table 8. Spectral Simulations

ID	exposure time (s)	power law χ^2	bremsstrahlung χ^2	blackbody and power law χ^2
		10% exposure time		
NGC 247 XMM1	1130	96.4/94	223.75/94	72.7/91
NGC 253 XMM1	10778	655.2/581	667.8/581	648.7/578
NGC 1313 XMM1	2789	188.7/201	189.08/201	187.2/197
NGC 1313 XMM2	2788	425.7/419	431.7/419	423.5/415
IC0342 XMM1	511	164.4/183	208.7/183	126/179
IC0342 XMM2	511	236.4/107	189.9/107	160.9/103
Holmberg II XMM1	982	1034.6/976	1152.1/976	971.2/972
M81 XMM1	9082	1314.4/1244	2010.9/1244	1246.1/1241
Holmberg IX XMM1	709	898.7/882	910.7/882	881.8/878
Circinus XMM2	9005	395.3/431	388.7/431	385.6/428
		5% exposure time		
NGC 247 XMM1	565	107.9/94	146.4/94	77/91
NGC 253 XMM1	5389	516.3/581	519.2/581	516.3/578
NGC 1313 XMM1	1394	125.8/201	125.9/201	122.9/197
NGC 1313 XMM2	1394	273.3/419	273.3/419	263.3/415
IC0342 XMM1	256	141.1/183	157.7/183	125.5/179
IC0342 XMM2	256	122.6/107	99.8/107	148/103
Holmberg II XMM1	491	908.3/976	981.8/976	871.3/972
M81 XMM1	4541	1086.8/1244	1426.2/1244	1060.7/1241
Holmberg IX XMM1	354	663.6/882	635.9/882	629.2/878
Circinus XMM2	4502	258.7/431	256.9/431	255.1/428

Table 9. *XMM-Newton* power law fit for best fit two-component spectra

Source	n_H[a]	Γ	χ^2/dof	F_X[c]	L_X[d]
NGC247 XMM1	$9.5^{+1.6}_{-1.4}$	$8.52^{+1.14}_{-0.91}$	112.2/95	1900	2200
NGC253 XMM1	$3.4^{+0.3}_{-0.3}$	$1.77^{+0.06}_{-0.06}$	262.6/232	3.1	3.6
...	$6.9^{+0.4}_{-0.4}$	$1.98^{+0.05}_{-0.05}$	611.6/582	2.9	3.3
NGC253 XMM2 (obs 2)	$2.2^{+0.1}_{-0.1}$	$2.03^{+0.04}_{-0.04}$	507.4/500	1.2	1.4
NGC253 XMM3	$3.9^{+0.5}_{-0.4}$	$2.17^{+0.14}_{-0.11}$	91.9/83	0.73	1.2
...	$4.0^{+0.4}_{-0.3}$	$2.06^{+0.09}_{-0.07}$	381.8/409	0.98	1.6
NGC253 XMM4	$8.5^{+3.0}_{-2.3}$	$2.09^{+0.33}_{-0.28}$	73.6/59	0.52	0.85
...	$1.2^{+0.3}_{-0.3}$	$2.09^{+0.16}_{-0.15}$	321.4/293	0.29	0.48
NGC253 XMM5	$1.7^{+1.2}_{-0.9}$	$1.54^{+0.22}_{-0.20}$	31.8/25	0.32	0.53
...	$3.4^{+0.2}_{-0.2}$	$2.17^{+0.7}_{-0.7}$	283.8/298	1.1	1.3
NGC253 XMM6	$3.9^{+0.3}_{-0.3}$	$2.21^{+0.84}_{-0.80}$	435/409	0.93	1.5
NGC253 XMM7	$7.1^{+0.7}_{-0.7}$	$2.15^{+0.11}_{-0.11}$	357/342	1.3	2.2
NGC300 XMM1	$0.97^{+0.11}_{-0.11}$	$2.67^{+0.06}_{-0.06}$	469.8/422	0.81	0.6
NGC300 XMM2	$1.7^{+0.40}_{-0.40}$	$3.20^{+0.32}_{-0.24}$	133.98/99	0.27	0.21
NGC300 XMM3	$3.4^{+0.8}_{-0.6}$	$1.86^{+0.15}_{-0.13}$	101.9/81	0.19	0.15
NGC300 XMM6	$?^{+?}_{-?}$	$2.05^{+0.17}_{-0.15}$	47.6/37	0.06	0.15
NGC1313 XMM1	$1.5^{+0.2}_{-0.2}$	$1.81^{+0.08}_{-0.09}$	219.8/203	0.42	0.88
NGC1313 XMM2	$2.8^{+0.16}_{-0.16}$	$2.48^{+0.07}_{-0.06}$	464.1/421	1.9	4.0
NGC1313 XMM3	$3.6^{+0.2}_{-0.2}$	$3.2^{+0.09}_{-0.09}$	778.3/426	3.3	6.9
IC0342 XMM3	$3.8^{+0.4}_{-0.4}$	$2.58^{+0.15}_{-0.14}$	185.8/109	1.7	3.1
NGC1705 XMM1	0.3^e	$1.93^{+0.11}_{-0.10}$	61.9/88	0.12	0.37
NGC1705 XMM2	$1.4^{+0.45}_{-0.41}$	$2.12^{+0.26}_{-0.15}$	91/76	0.078	0.24
NGC1705 XMM3	$0.6^{+0.36}_{-0.40}$	$1.36^{+0.12}_{-0.13}$	80.9/67	0.17	0.53
NGC2403 XMM1	$3.2^{+0.61}_{-0.55}$	$2.15^{+0.16}_{-0.15}$	92.2/81	2.2	3.6
NGC2403 XMM2	$2.7^{+0.37}_{-0.34}$	$2.07^{+0.11}_{-0.11}$	179.5/151	1.3	2.0
NGC2403 XMM3	$1.9^{+0.40}_{-0.36}$	$1.97^{+0.14}_{-0.13}$	92.6/107	0.81	1.3
HolmII XMM1 (obs 1)	$1.5^{+0.07}_{-0.07}$	$2.61^{+0.04}_{-0.04}$	1134.2/976	12	10
Holm I XMM1	$?^{+?}_{-?}$	$2.04^{+0.14}_{-0.07}$	102.8/95	0.48	1.7
M81 XMM1	$3.2^{+0.07}_{-0.07}$	$2.09^{+0.02}_{-0.02}$	1849.9/1245	4.5	7.0
...	$3.0^{+0.3}_{-0.3}$	$1.79^{+0.07}_{-0.07}$	224.9/208	4.3	6.7
M81 XMM2	7.3	6.13	1358.2/618	48.5	75.2
M81 XMM3	$0.97^{+0.25}_{-0.41}$	$1.58^{+0.18}_{-0.15}$	81.35/80	2.5	3.9
M81 XMM4	$?^{+?}_{-?}$	$0.88^{+0.11}_{-0.11}$	66.4/52	0.35	0.54
M81 XMM5	$1.0^{+0.4}_{-0.3}$	$1.52^{+0.11}_{-0.11}$	97.5/82	0.44	0.68
Holm IX XMM1	$1.7^{+0.08}_{-0.08}$	$1.84^{+0.03}_{-0.03}$	1000.9/882	9.4	15
NGC4214 XMM2	$0.2^{+0.5}_{-0.2}$	$2.03^{+0.43}_{-0.28}$	50.9/46	0.16	0.14
NGC4258 XMM1	$1.6^{+0.4}_{-0.4}$	$1.9^{+0.14}_{-0.13}$	101.4/78	0.06	0.04
NGC4258 XMM2 (obs 1)	$3.5^{+0.9}_{-0.7}$	$1.88^{+0.16}_{-0.15}$	97.5/63	0.43	2.6
NGC4395 XMM1	$3.7^{+0.5}_{-0.4}$	$4.93^{+0.34}_{-0.30}$	195.1/156	7.2	14
NGC4395 XMM3	$?^{+?}_{-?}$	$1.86^{+0.14}_{-0.09}$	55.9/58	0.25	0.48
NGC4449 XMM3	$3.3^{+0.5}_{-0.4}$	$3.36^{+0.29}_{-0.23}$	154/89	1.3	1.5
NGC4490 XMM1	$0.83^{+0.14}_{-0.12}$	$2.53^{+0.17}_{-0.16}$	101.5/65	1.2	8.7
NGC4490 XMM2	$6.3^{+1.3}_{-1.0}$	$2.36^{+0.19}_{-0.17}$	49.5/56	0.92	6.7
NGC4490 XMM3	$9.4^{+1.5}_{-1.2}$	$2.95^{+0.24}_{-0.20}$	76.7/80	1.5	11
NGC4631 XMM1	$2.3^{+0.16}_{-0.15}$	$2.13^{+0.06}_{-0.05}$	383.4/347	0.76	5.1
NGC4631 XMM2	$1.9^{+0.4}_{-0.3}$	$2.01^{+0.14}_{-0.12}$	119.5/99	0.23	1.5

Table 9—Continued

Source	n_H[a]	Γ	χ^2/dof	F_X[c]	L_X[d]
NGC4631 XMM3	$0.63^{+0.3}_{-0.2}$	$1.53^{+0.1}_{-0.08}$	146/98	0.15	1.0
NGC4945 XMM1	$5.8^{+0.8}_{-0.7}$	$1.88^{+0.08}_{-0.10}$	116/122	0.9	1.0
NGC4945 XMM2	$3.4^{+0.6}_{-0.5}$	$1.58^{+0.09}_{-0.10}$	114.5/115	0.71	0.82
NGC4945 XMM4	$5.2^{+0.8}_{-0.7}$	$2.59^{+0.19}_{-0.17}$	75.5/62	0.49	0.56
NGC5204 XMM1	$0.61^{+0.1}_{-0.1}$	$2.11^{+0.04}_{-0.04}$	621.4/561	2.0	5.5
$\cdots$	$1.1^{+0.1}_{-0.1}$	$2.41^{+0.07}_{-0.07}$	626.9/498	3.0	8.3
M51 XMM2	$2.3^{+0.50}_{-0.30}$	$2.50^{+0.22}_{-0.20}$	75.2/70	0.52	3.3
M51 XMM5	2.7	3.08	256.0/72	0.43	2.7
M51 XMM7	$0.5^{+0.39}_{-0.46}$	$1.95^{+0.23}_{-0.18}$	37.8/31	0.11	0.66
M83 XMM1	$1.9^{+0.34}_{-0.31}$	$2.32^{+0.13}_{-0.12}$	210.9/211	0.64	2.8
M83 XMM4	$4.4^{+1.3}_{-0.9}$	$2.30^{+0.20}_{-0.18}$	107.5/91	0.4	1.8
M101 XMM1	$0.56^{+0.15}_{-0.14}$	$1.98^{+0.08}_{-0.08}$	303/233	0.45	2.9
M101 XMM2	$2.2^{+0.25}_{-0.23}$	$1.85^{+0.07}_{-0.07}$	288.8/263	0.81	5.3
M101 XMM4	$2.2^{+0.45}_{-0.42}$	$2.25^{+0.20}_{-0.17}$	165.7/140	0.38	2.5
NGC5408 XMM1	$1.6^{+0.2}_{-0.1}$	$3.57^{+0.12}_{-0.11}$	396.8/339	7.04	19.4
CIRCINUS XMM1	$7.6^{+0.3}_{-0.3}$	$2.15^{+0.05}_{-0.04}$	762.9/863	4.6	8.8
CIRCINUS XMM2	$11.7^{+0.4}_{-0.7}$	$3.48^{+0.13}_{-0.06}$	517.9/432	2.7	5.2
CIRCINUS XMM3	$9.0^{+2.1}_{-1.0}$	$2.57^{+0.40}_{-0.17}$	285.2/262	0.32	0.61

[a]total column density in units of 10^{21} cm^{-2}

[b]improvement in χ^2 over the single-component power law model

[c]unabsorbed flux in the 0.3-10 keV band in units of 10^{-12} erg cm^{-2} s^{-1}

[d]unabsorbed luminosity in the 0.3-10 keV band, using the distances quoted in Table 1, in units of 10^{39} erg s^{-1}

[e]absorption level frozen at approximate galactic level

Table 10. Best-Fit Absorbed Comptonization Model Parameters

ID	nH[a]	kT[b]	tau[c]	χ^2	F_X[d]
NGC 253 XMM2	$1.8^{+0.08}_{-0.16}$	$1.28^{+0.13}_{-0.12}$	$19.59^{+2.0}_{-1.6}$	464/498	1.47
NGC 2403 XMM1	$1.95^{+1.2}_{-0.6}$	$0.98^{+0.16}_{-0.15}$	$25.4^{+7.2}_{-8.3}$	82.8/85	1.4
NGC 4490 XMM1	$4.7^{+1.1}_{-2.1}$	$0.96^{+0.13}_{-0.16}$	$27.0^{+18.3}_{-4.9}$	66.5/64	0.66
NGC 4490 XMM2	$5.0^{+1.6}_{-1.4}$	$1.21^{+0.21}_{-0.31}$	$18.8^{+8.6}_{-9.7}$	45.7/55	0.67
M101 XMM2	$1.6^{+0.26}_{-0.24}$	$1.24^{+0.09}_{-0.15}$	$23.3^{+3.4}_{-2.8}$	256/262	0.65
M101 XMM3	$1.1^{+0.43}_{-0.40}$	1.13	15.2	128/132	0.41
Circinus XMM2	$6.8^{+1.3}_{-0.9}$	$0.62^{+0.08}_{-0.04}$	$29.7^{+8.1}_{-7.0}$	437.2/430	0.5
Circinus XMM3	$6.7^{+1.6}_{-2.4}$	$0.93^{+0.28}_{-0.24}$	$23.1^{+17.5}_{-5.2}$	273.1/261	0.17

[a]total column density in units of 10^{21} cm^{-2}

[b]temperature in keV

[c]optical depth

[d]unabsorbed flux in the 0.3-10 keV band in units of 10^{-12} erg cm^{-2} s^{-1}

Table 11. *XMM-Newton* Galaxy Observations

Galaxy	S_{60} (Jy)	S_{100} (Jy)	F_{FIR}[a]	L_{FIR}[b]	No. of ULX
NGC247	7.93	27.32	0.602	0.687	1
NGC253	998.73	1861.67	55.92	93.10	3
NGC300	23.08	74.45	1.688	1.324	0
NGC625	5.09	9.08	0.280	0.230	0
NGC1313	35.97	92.00	2.329	4.845	2
IC0342	255.96	661.68	16.66	30.32	3
NGC1569	45.41	47.29	2.072	0.635	0
NGC1705	0.970	2.580	0.064	0.199	0
MRK 71	3.51	4.67	0.173	0.239	0
NGC2403	51.55	148.49	3.547	5.378	2
Holmberg II	1.15	2.62	0.070	0.061	1
Holmberg I	$\cdots$	$\cdots$	$\cdots$	$\cdots$	1
M81	44.73	174.02	3.647	5.655	1
M82	1271.32	1351.09	58.35	106.2	1
Holmberg IX	$\cdots$	$\cdots$	$\cdots$	$\cdots$	1
Sextans A	0.255	0.674	0.017	0.004	0
IC 2574	2.41	10.62	0.212	0.329	0
NGC 4214	17.87	29.04	0.947	0.826	1
NGC 4258	21.60	78.39	1.690	10.48	1
NGC4395	4.21	12.90	0.299	0.573	1
NGC4449	37.00	58.28	1.937	2.199	2
NGC4490	47.79	85.94	2.636	19.19	5
NGC4631	82.90	208.66	5.324	35.83	1
NGC4736	62.41	135.34	3.734	8.261	4
NGC4945	588.11	1415.5	36.95	42.49	0
NGC 5204	2.33	5.35	0.143	0.395	2
M51	108.68	292.08	7.213	44.74	5
M83	266.03	638.63	16.69	76.79	0
NGC5253	30.00	30.92	1.365	16.72	0
M101	88.04	252.84	6.048	39.63	4
NGC5408	2.825	2.958	0.129	0.356	1
Circinus	248.7	315.85	12.06	23.10	4

[a] flux in units of $10^{-9} \, \mathrm{erg \, cm^{-2} \, s^{-1}}$

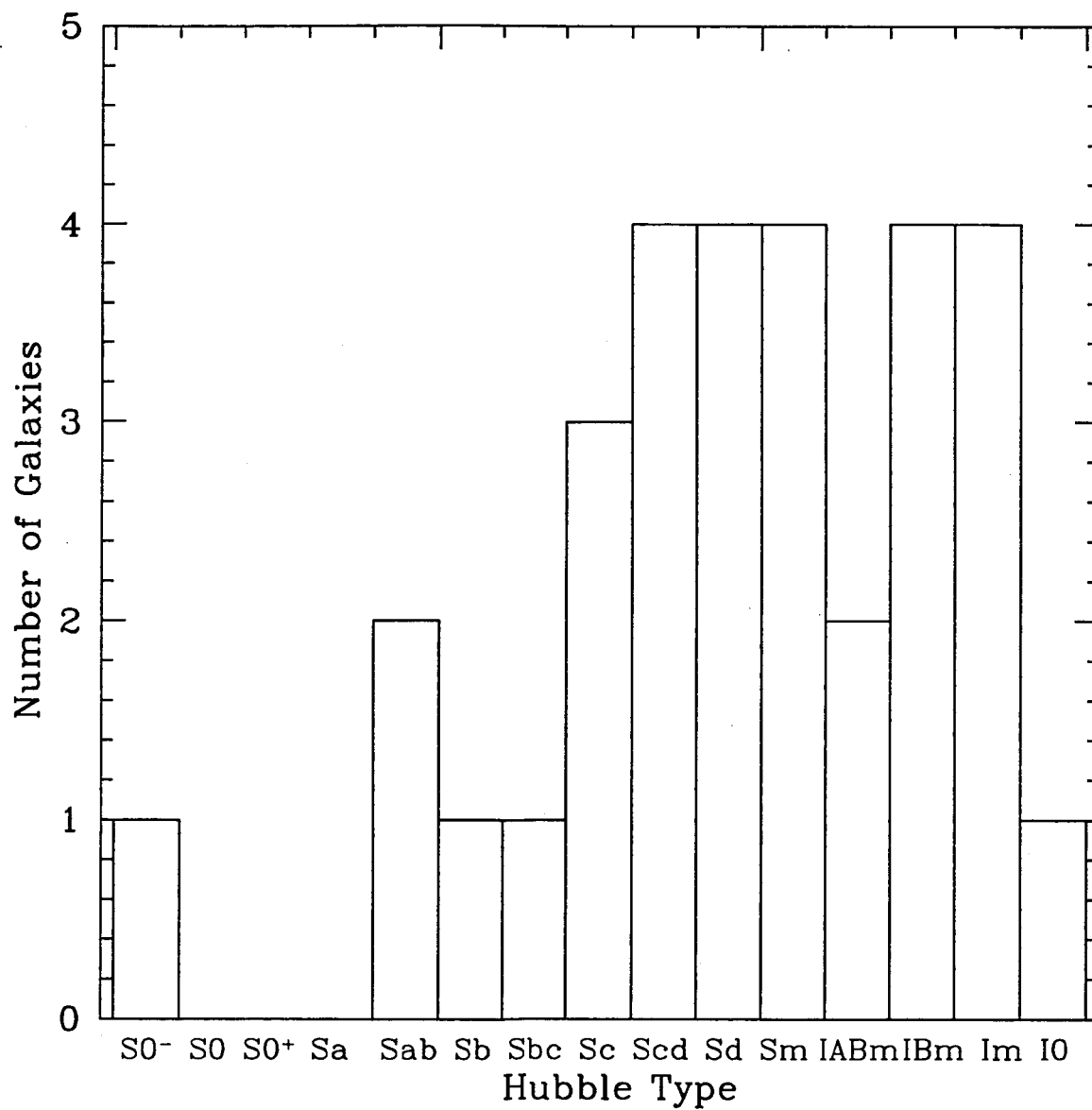[b] far-infrared luminosity in units of $10^{42} \, \mathrm{erg \, s^{-1}}$

Fig. 1.— Distribution of galaxies by Hubble type among our archival *XMM-Newton* sample of nearby (< 8 Mpc) galaxies. Our sample consists solely of spirals and irregulars.
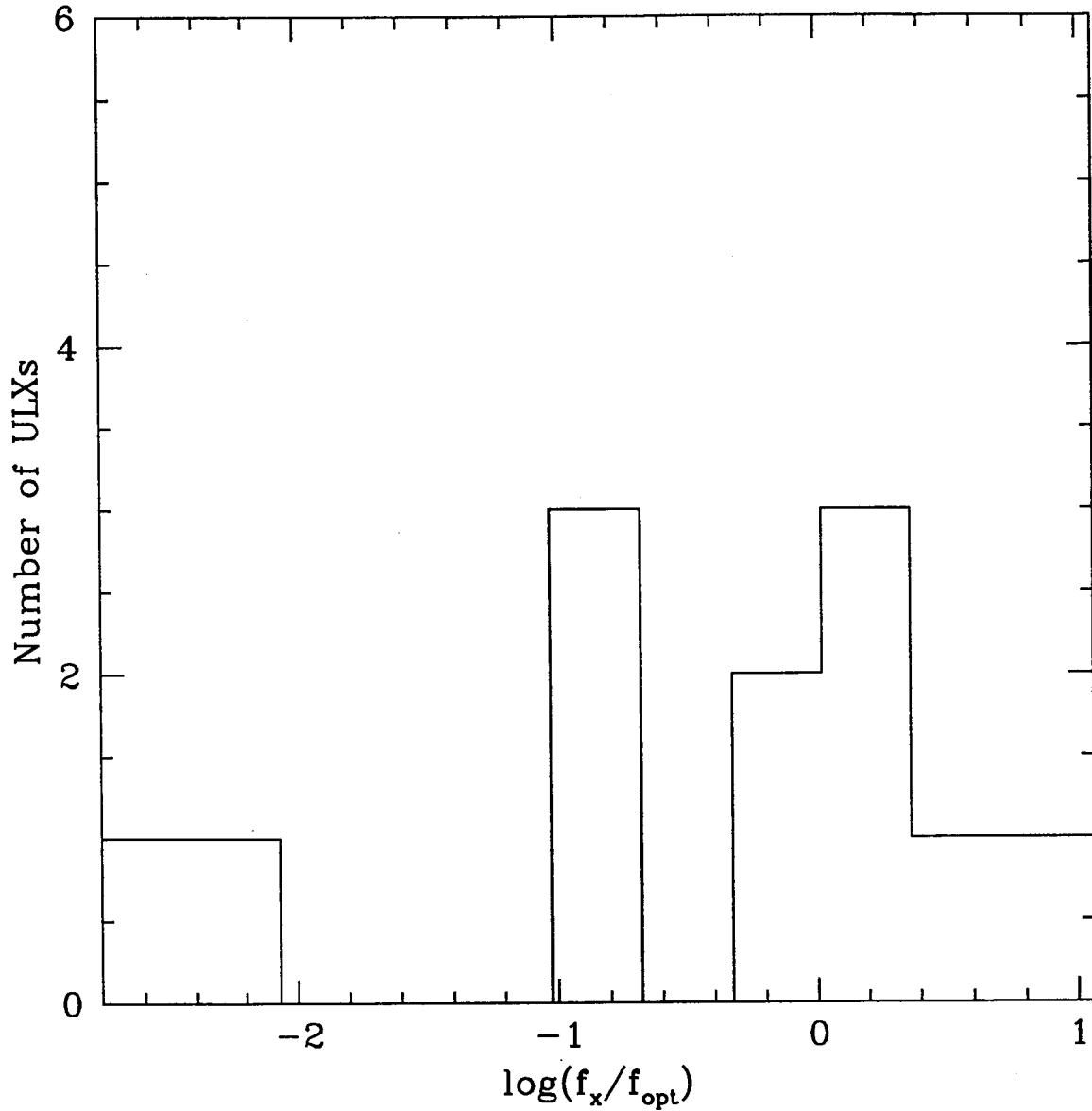
Fig. 2.— The distribution of f_x/f_{opt} for the brightest possible optical point source within the *XMM-Newton* error circle. We define f_x as the unabsorbed X-ray flux in the $0.3 - 10\,\mathrm{keV}$ range and f_{opt} as the optical flux obtained from the U filter of *XMM*'s OM (as described in text). These ratios do not represent the actual f_x/f_{opt} of the sources but are an estimate of the maximum possible value. A majority of the sources had no optical point source within the X-ray contour and thus have ratios of f_x/f_{opt} far higher than those indicated in the plot.
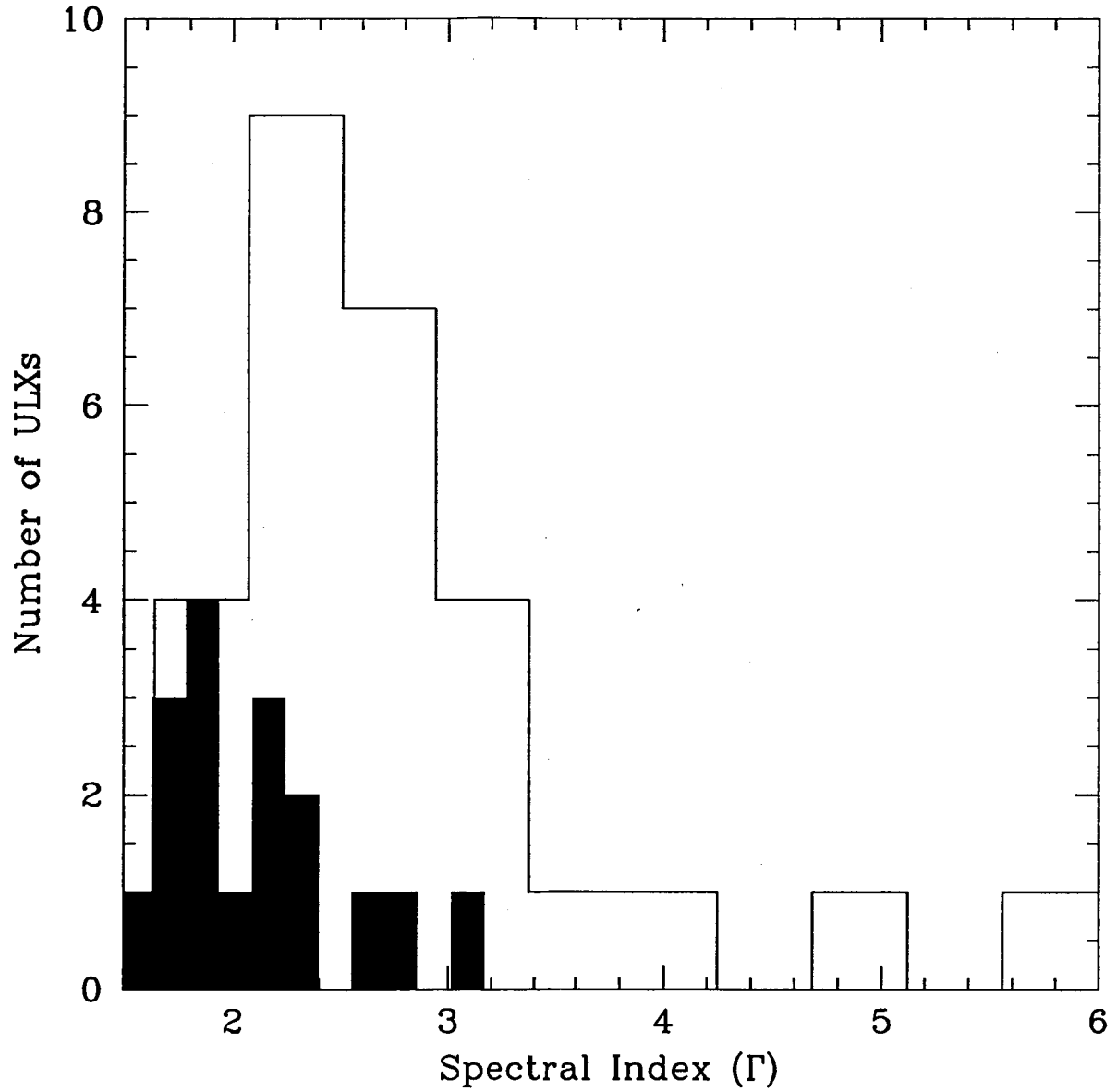
Fig. 3.— Distribution of the spectral indices (Γ) for low-state (shaded) and high-state (open) objects. For Galactic low-state objects, typically $\Gamma \approx 2.0$, similar to our sample, while the high-state objects have a steeper Γ (McClintock & Remillard 2004).
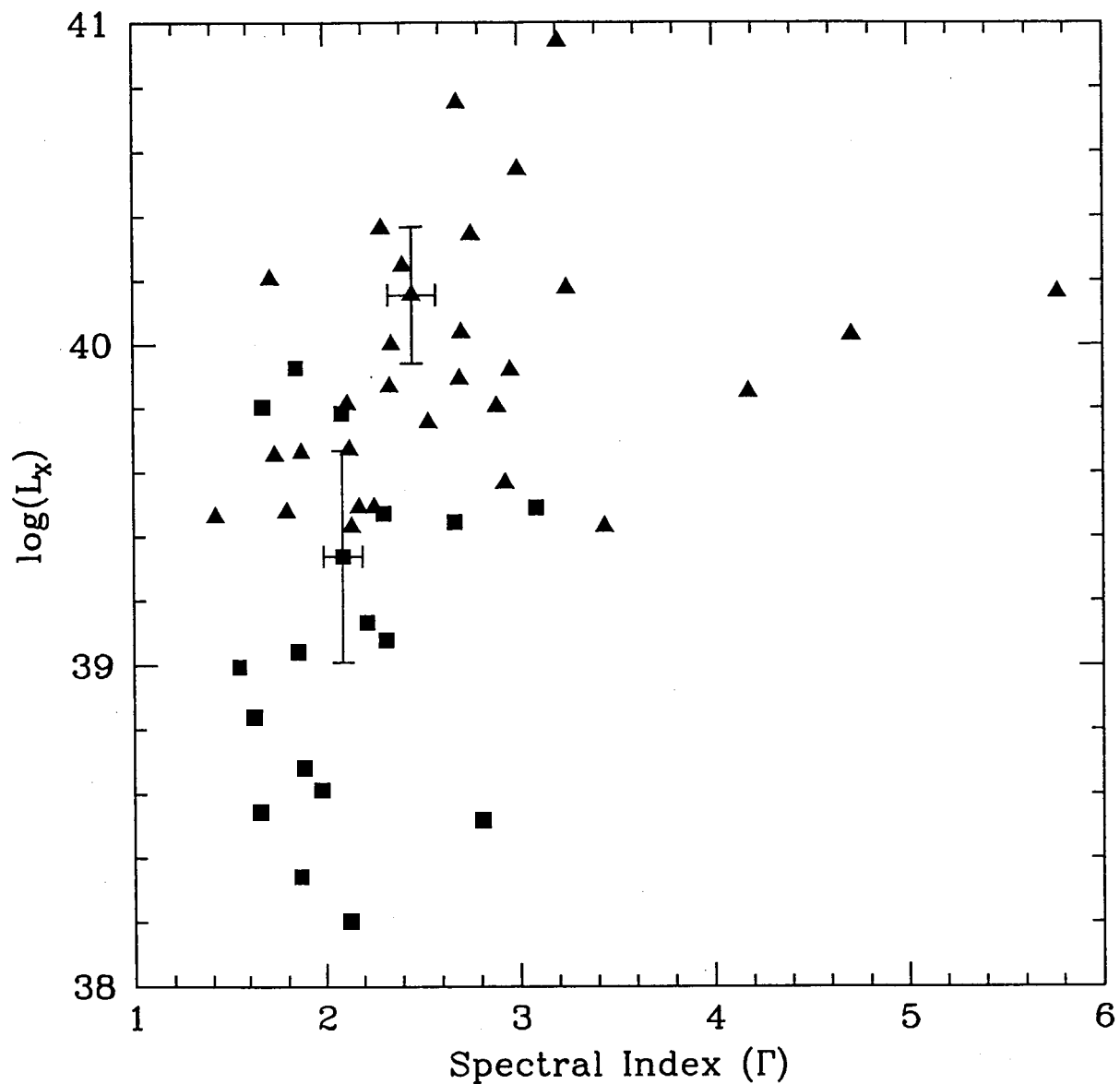
Fig. 4.— Relationship of luminosity vs. spectral index for low-state (rectangle) and high-state (triangle) objects. As expected from observations of Galactic stellar-mass black hole systems (Mc-Clintock & Remillard 2004), the classified low-state ULXs in our sample have, on average, lower X-ray luminosities than the corresponding high-state ULXs. We plot the mean values for both high-state and low-state objects with errorbars indicating the root mean square deviation. The outlying objects with spectral indices greater than 3.5 were not included in the mean or deviation calculations.
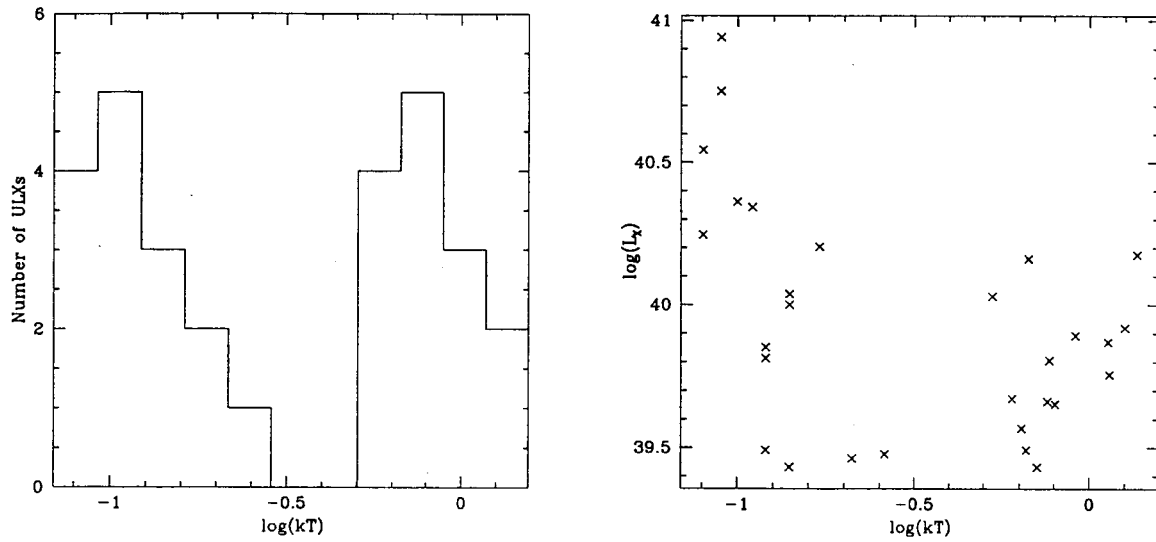
Fig. 5.— (left)Distribution of the blackbody temperature for high-state objects.(right)Relationship of blackbody temperature vs. luminosity (in the 0.3-10 keV band) for high-state objects. We see two peaks arise in the distribution, one centered around kT≈ 0.1 and another at kT≈ 1. The peak with a low disk temperature also corresponds to the highest luminosities, suggesting that these may be high-state IMBHs. The sources with higher disk temperature also have lower luminosities. The spectra of these sources were also well fit by an inverse Comptonization model (a model succesfully used to fit some of the Galactic black hole X-ray binaries in the very high state).
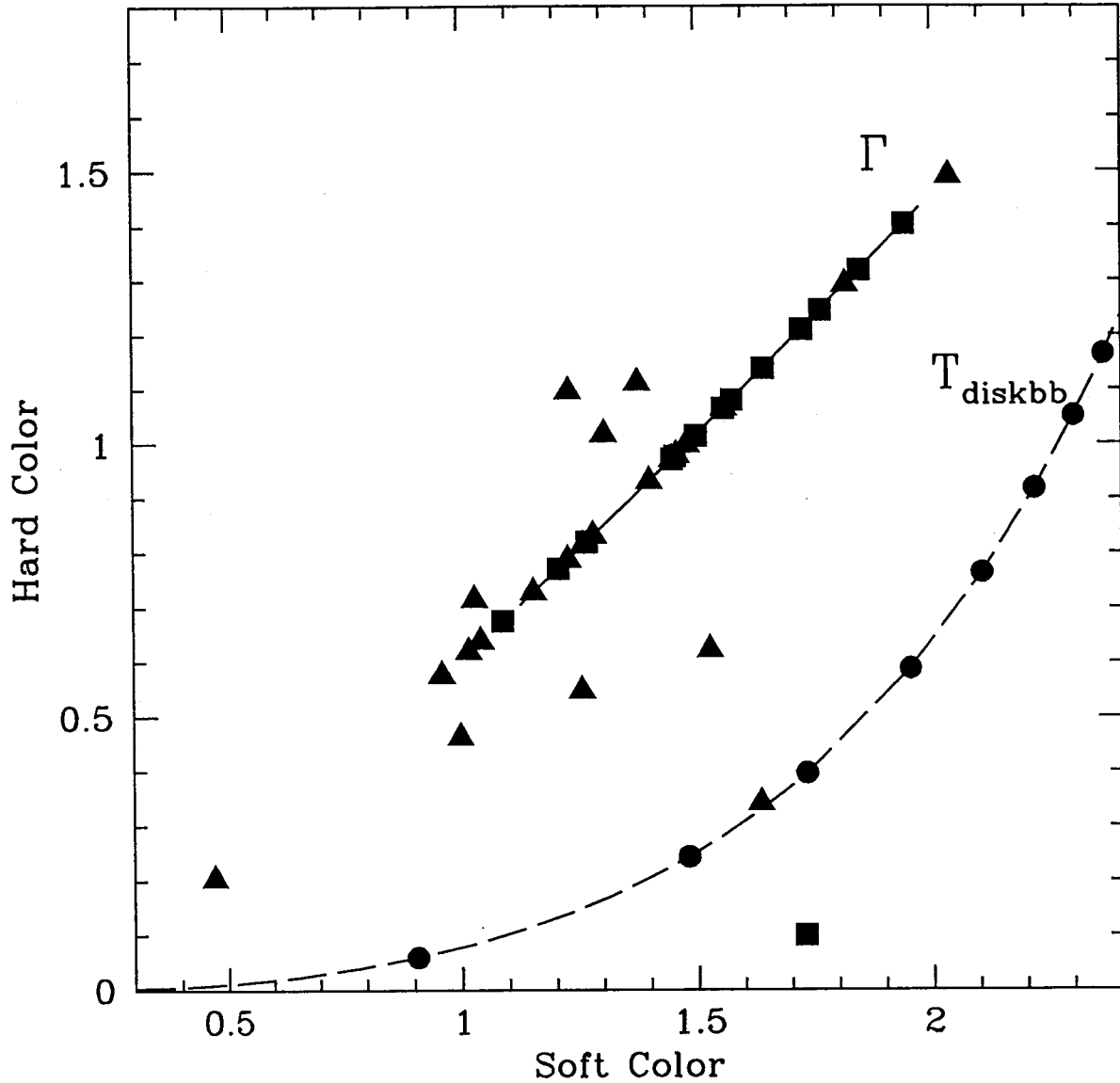
Fig. 6.— Color-Color Diagram plotting soft vs. hard colors, as outlined in Done & Gierlinski (2003), for low-state (rectangle) and high-state (triangle) ULXs. A large number of our sources lie in the same range of this graph as the black hole sources examined by Done & Gierlinski (2003) (near the power law distribution, indicated by the solid line). The dashed line represents the color-color plot for a multi-colored disk model with different disk temperatures. The sources approaching this line were those well-fit by the Comptonization model. Done & Gierlinski (2003) had no black hole sources in this region, but atolls and Z-sources, which were also well-fit by Comptonization models.
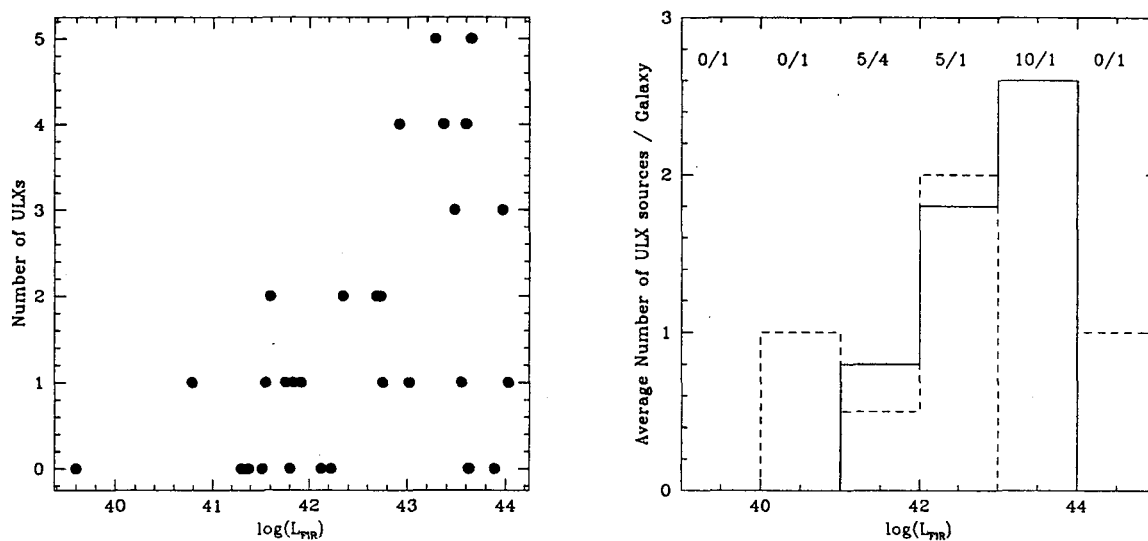
Fig. 7.— (left) Relationship of the far-infrared luminosity, as an indicator of star formation rate, vs. the number of ULXs for each galaxy. If ULXs are associated with star formation, we naively expect that the higher the FIR luminosity the more ULXs the galaxy will host. (right) The distribution of average number of ULXs / L_{FIR} bin for spirals (solid line) follows this expectation. The distribution of irregulars (dashed line) is not so easily interpreted. The numbers at the top indicate the number of spirals/irregulars in each of the luminosity bins. More irregulars would need to be included in this survey for meaningful statistics on this group.
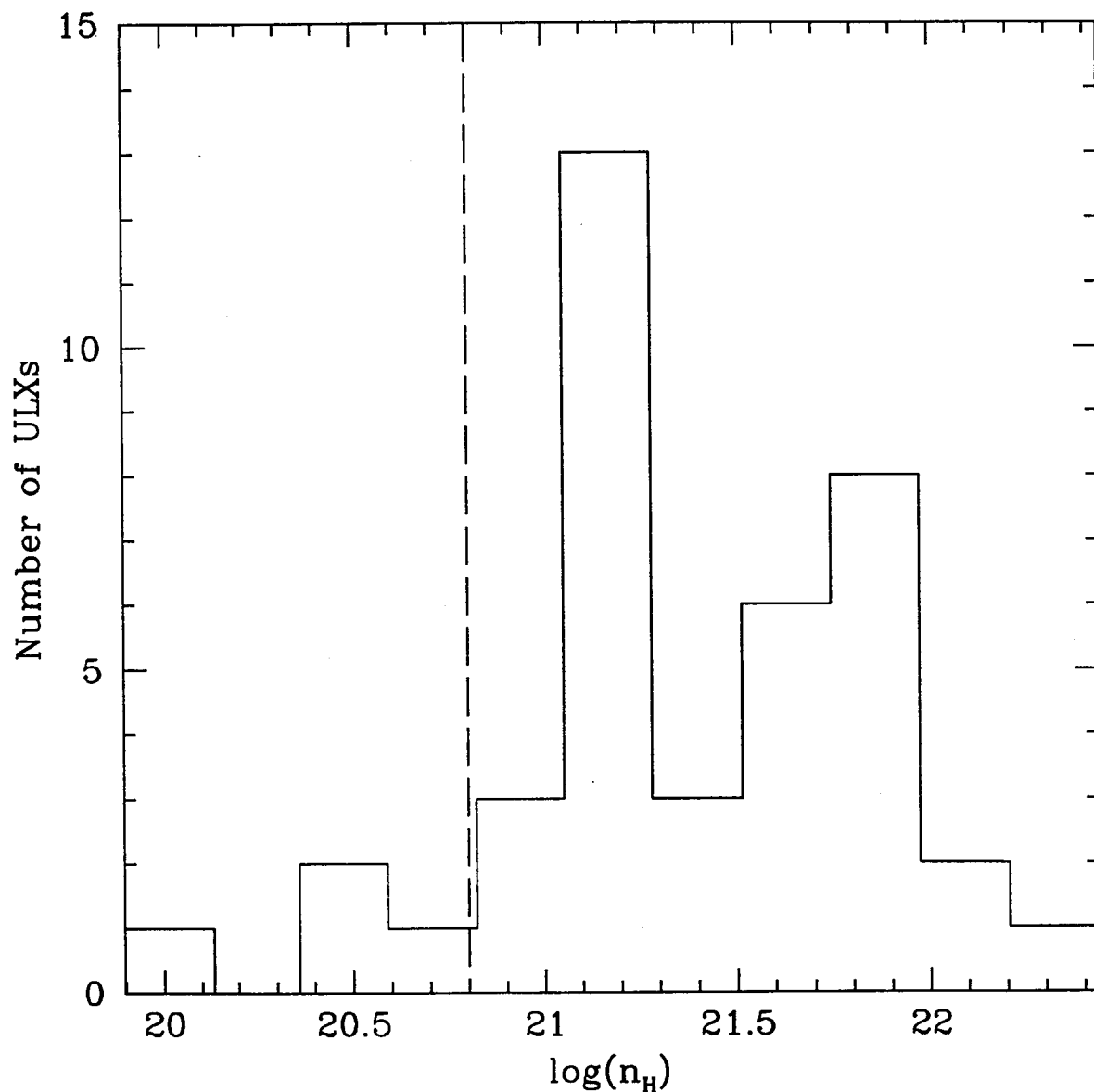
Fig. 8.— Distribution of the hydrogen column densities of ULX sources. The n_H values were obtained through spectral fits using the *wabs* model in *XSPEC*. Galactic column densities towards the host galaxy were subtracted from the spectral fit values. A majority of our ULX sources have high column densities ($> 10^{21} cm^{-2}$), suggesting that some of this absorption originates with the local ULX environment. Bins to the left of the dashed line represent sources with column densities very close to the Galactic value and thus a simple subtraction is not statistically representative of the true value.